Atomistic TCR-ligand interactions instruct memory T-cell differentiation

Aoi Akitsu[1,2,3], Kemin Tan[4], Robert J. Mallis[1,2,3,5], Matthew A. Booker[6], Jonathan S. Duke-Cohan[1,2,3], Kristine N. Brazin[1,2,3], Evan H. Kirkpatrick[7], Andrew N. Parkins[1,2,3], Sarita Aryal[1,2,3], Vincenzo Cinella[1,2], Jonathan J. Lee[1,2], Kaveri I. Uberoy[1,2], Jenna K. Koenig[1,2], Matthew Biddle[1,2], Cameron M. Messier[8], Patrick H. Lizotte[8], Michael Y. Tolstorukov[6], Wonmuk Hwang[9,10], Matthew J. Lang[7,11]*, Ellis L. Reinherz[1,2,3]*

[1]Laboratory of Immunobiology, Dana-Farber Cancer Institute; Boston, MA 02115, USA.
[2]Department of Medical Oncology, Dana-Farber Cancer Institute; Boston, MA 02115, USA.
[3]Department of Medicine, Harvard Medical School; Boston; MA 02115, USA.
[4]Structural Biology Center, X-Ray Science Division, Advanced Photon Source, Argonne National Laboratory; Lemont, IL 60439, USA.
[5]Department of Dermatology, Harvard Medical School; Boston, MA 02115, USA.
[6]Department of Informatics and Analytics, Dana-Farber Cancer Institute; Boston, MA 02115, USA.
[7]Department of Chemical and Biomolecular Engineering, Vanderbilt University; Nashville, TN 37212, USA
[8]Belfer Center for Applied Cancer Science, Dana-Farber Cancer Institute; Boston, MA, USA.
[9]Departments of Biomedical Engineering, Materials Science & Engineering, Physics & Astronomy, Texas A&M University; College Station, TX 77843, USA
[10]Center for AI and Natural Sciences, Korea Institute for Advanced Study; Seoul 02455, Republic of Korea
[11]Department of Molecular Physiology and Biophysics; Vanderbilt University School of Medicine; Nashville, TN 37232, USA
*Corresponding authors. Email: ellis_reinherz@dfci.harvard.edu, matt.lang@vanderbilt.edu

Summary

Memory T cells endow the mammalian host with an essential form of adaptive immunity that generates durable and rapid protection following re-exposure to an infectious pathogen or a cancerous transformation[1-4]. How naive CD8$^+$ T cells develop into memory T cells that bifurcate into long-lived central (T_{CM}) versus effector (T_{EM}) subsets after such an antigen encounter remains ill-defined at the molecular level. To address this gap, here we dissect the functional T-cell receptor (TCR) repertoire of 242 murine CD8$^+$ TCRαβ clonotypes specific for the peptide-major histocompatibility complex molecule (pMHC) comprising an immunodominant influenza A virus (IAV) oligopeptide epitope $NP_{366–374}$ presented by H-2D^b [5,6]. Using single-cell transcriptomics with TCR sequencing, biophysical measurements of force-dependent TCR-pMHC interactions, *in vivo* memory development, and structural analyses, we integrate these data to define relationships between signaling polarity and memory fate. We find that T_{CM} and T_{EM} polarities are reflected in distinct subunit-related mechanotransduction biases: T_{CM}-associated TCRs favor TCRβ-driven pMHC engagement, whereas T_{EM}-associated TCRs preferentially favor TCRα-driven pMHC engagement. Moreover, "bipolar" clonotypes (T_{BP}) capable of generating both memory subsets exhibit more balanced signaling, the largest average clonal expansions, and broadest heterosubtypic crossreactivities. By contrast, variegated T_{CM} TCR sequences foster mostly clonal singlets with the greatest IAV mutant recognition potential within the overall memory repertoire, thus revealing two complementary memory niche crossreactivity strategies. Weak, force-sensitive TCR bonds are pervasive for this entire repertoire, being most conspicuous amongst T_{CM} clonotypes. At the atomic level, highly nuanced variation in TCRαβ bonding to either peptide and/or MHC modulates mechanical load transmission across the holoreceptor's ectodomains, transmembrane segments, and CD3 cytoplasmic tails to differentially influence downstream tyrosine phosphorylation and memory development. Collectively, TCR diversity anticipates epitope-specific pathogen evolution, whereas divergent TCR signaling regulates memory fate with implications for adoptive T-cell immunotherapies seeking to maximize persistence and minimize functional exhaustion.

Introduction

Immunological memory is a hallmark of the adaptive immune system, enabling rapid and robust targeted responses upon re-exposure to pathogens or tumors. $CD8^+$ T cells play a central role in this process by first recognizing threats through their clone-specific (clonotypic) TCRs and then eliminating infected or malignant cells by elaborating cytotoxic molecules and cytokines. Following acute viral infection, a small population of effector $CD8^+$ T cells that survive the predominant contraction phase differentiates into long-lived memory cells to provide durable protection [1,2]. Memory $CD8^+$ T cells are functionally and phenotypically heterogeneous but broadly classified into two circulating lymphocyte subsets, termed central memory (T_{CM}) and effector memory (T_{EM}) cells [3]. A non-circulating subset of tissue-resident memory T cells (T_{RM}) also forms [4]. T_{CM} and T_{EM} cells differ in surface markers, migratory behavior, functional potential, and transcriptional and epigenetic landscapes [4]. T_{CM} cells express lymphoid-homing receptors such as CD62L and CCR7, enabling their lodging in secondary lymphoid organs. They also express transcription factors including Tcf1 [7], Lef1 [8], and Id3 [9] which support T_{CM}-like properties such as self-renewal, long-term persistence, and a robust proliferative response upon antigen re-encounter [10,11]. In contrast, T_{EM} cells lack CD62L and CCR7, allowing them to circulate through the blood and access both lymphoid and non-lymphoid tissues. They preferentially express Id2 [12,13], which promotes effector differentiation, and are enriched for cytotoxic mediators such as granzyme B (Gzmb) and granzyme K (Gzmk), positioning them as a frontline defense capable of exerting immediate effector function [1,3].

The generation of memory subsets during viral infection is believed to be shaped by both extrinsic factors such as antigen abundance, inflammatory cytokines, and the tissue microenvironment as well as intrinsic transcriptional regulators and metabolic programs [1,14,15]. How memory fate is ultimately determined, however, remains unresolved. Notwithstanding, three conceptual models have been proposed [1]. The first, the intrinsic memory T cell fate model, suggests that fate is imprinted in naïve T cells prior to activation, i.e. the TCR *per se* directs memory T cell development. The second, the linear differentiation model, suggests that memory precursor cells (T_{MP}) give rise to memory subsets sequentially from T effector cells (T_{EFF}) to T_{EM} followed by T_{CM}, with the latter especially pronounced in the context of high precursor frequencies [10,16-18]. The third, so-called signal strength model, alternatively posits that the intensity of TCR and co-stimulatory signaling during priming governs fate decisions, with stronger signals promoting T_{EM} differentiation and weaker signals favoring T_{CM} [19-21]. These models are largely based on several TCR transgenic systems, with or without altered peptide ligands (APLs) utilized to tune TCR signal strength. While elegant, these systems cannot recapitulate the diversity of TCRs and T-cell competition operative in the mammalian repertoire.

As recent studies have shown that TCR ligand recognition specificity and sensitivity are regulated by T-cell sensing of physical load placed on a TCR-pMHC bond during immune surveillance [5,22-32], we examined the biophysical and structural contributions of this mechanosensing to intrinsic CD8 memory fate within a single TCR repertoire. Our results indicate that memory T_{EM} and T_{CM} differentiation is unrelated to TCR signaling threshold performance metrics. Instead, differentiation "polarity" is dependent upon disparate signaling linked to the structural features of the TCR-pMHC interaction, including bonding and surface topology

involving dynamic TCR behaviors under force that impact mechanotransduction. These attributes define an atomistic basis for divergence amongst TCRs differing by as few as 1-3 amino acids.

Results

TCR clonotypes of varying T-cell burst sizes and polarities

To investigate whether αβTCRs *per se* impact memory T cell subset fate, we performed single-cell RNA Sequence (scRNA-seq) on $NP_{336-374}/D^b$-specific CD8 T cells isolated from pooled mediastinal lymph nodes (mLNs) of 10 B6 mice at 34 days post-IAV infection (dpi 34) using the mouse-adapted A/Puerto Rico/8/1934 (PR8) strain (Extended Data Fig. 1a). A total of 5,429 CD8 T cells comprising 242 clonotypes with paired TCRα and TCRβ V domain sequences were identified. Uniform Manifold Approximation and Projection (UMAP) analysis revealed two major clusters corresponding to central memory CD8 T cells (T_{CM}) and effector memory CD8 T cells (T_{EM}), appearing as left- and right-sided lobulated aggregates, respectively, (Fig. 1a). Furthermore, differentially expressed genes (DEGs) and hierarchical clustering (Supplementary Data 1 and Extended Data Fig. 1b) discriminated three distinct T_{CM} clusters and three T_{EM} clusters. Of the former, $T_{CM\text{-}CONV}$ (T_{CMC}) expressed conventional T_{CM} genes (*Klf2, Id3, Tcf7, Ccr7*), $T_{CM\text{-}XCL1}$ (T_{CMX}) specifically expressed *Xcl1, Cxcl10, and Mif*, and $T_{CM\text{-}PRO}$ (T_{CMP}) was enriched for proliferative genes (histone-related genes, *Stmn1, Pclaf, Birc5, and Ube2x*). With respect to the T_{EM}, $T_{EM\text{-}CONV}$ (T_{EMC}) cluster expressed conventional T_{EM} genes (*Gzmb, Gzmk, Id2, Ccl5*), $T_{EM\text{-}KLR}$ (T_{EMK}) was enriched for KLR genes (*Klrd1 and Klrc1*), and $T_{EM\text{-}EXH}$ (T_{EME}) expressed exhaustion-associated genes (*Pdcd1*, *Lag3*, *Havcr2*). Selected top genes are shown in Fig. 1b. Independent gene signatures derived from T_{CM} and T_{EM} clusters, identified by separate scRNASeq analysis on $CD8\beta^+CD44^+$ memory cells isolated by FACS from pooled mLNs of four B6 mice at dpi 33 (Methods) validated the transcriptional identity of these subsets specifically in the IAV context (Fig. 1c and Extended Data Fig. 2a). Interestingly, *Sell*-encoded CD62L, a canonical T_{CM} cell surface marker, was weakly expressed even within the T_{CM} cluster, as reflected by the low frequency on $NP_{366-374}/D^b$-specific memory $CD8^+$ T cells (Extended Data Fig. 2b,c), compared to the level on $PA_{224-233}/D^b$-, and $PB1_{703-711}/K^b$-specific $CD8^+$ T cells. Hence, the expression of classical memory subset markers is apparently modulated in an epitope-specific manner.

We analyzed the distribution of clonotypes across the UMAP clusters to determine whether TCRs significantly influence memory fate (Fig. 1d), identifying those with single TCRα and TCRβ chains after filtration (Supplementary Data 2 and Methods). Among the top 40 clonotypes, 25 were distributed comparably amongst subsets of T_{CM} vs T_{EM} clusters. In contrast, the remaining 15 clonotypes were highly skewed toward one or the other subsets, suggesting that TCRs *per se* impact memory T cell fate as indicated by the low adjusted p-values (Fig. 1e and Supplementary Table 1). Accordingly, clonotypes were categorized as belonging to the T_{CM} vs T_{EM} type when >70% of the cells in each clone's progeny were polarized toward one or more of the three respective subclusters therein, as defined in Fig. 1a. Other clonotypes with a more equivalent distribution not achieving the 70% threshold were classified as bipolar (T_{BP}). Representative clonotypes listed in Fig. 1e underwent further analysis. The NP41, as well as NP34 and NP63,

166 TCRs identified in a previous study of the IAV memory recall response [5] were also observed here
167 in the primary memory pool, as one T_{CM} and two T_{BP} clonotypes, respectively. Moreover, since
168 both analogue NP34 and digital NP63 are categorized as T_{BP}, their different performance under
169 pN forces (i.e. digital TCRs need only a few pMHC for activation while analogue TCRs require
170 dozens to hundreds), is not linked to the T memory subset determination. The cell projection on
171 the UMAP (Fig. 1f) and the Euclidean distance of principal component-1 (PC1) for NP201, NP204,
172 and NP207 (Fig. 1g) confirmed their locations in $T_{CM,}$ $T_{EM,}$ or both clusters, highlighting gene
173 expression similarity between individual clonotypes and the overall T_{CM} and T_{EM} populations as
174 well as total T cells.
175
176 We further examined the localization of all cell types belonging to each memory clonotype
177 category (CT) and projected their distribution on the UMAP of the entire CD8 repertoire (Fig. 1h).
178 "CT-matched" cells (i.e., T_{CM} cells in T_{CM} CTs and T_{EM} cells in T_{EM} CTs) are localized primarily
179 toward the periphery of the respective T_{CM} and T_{EM} regions, whereas T_{CM} and T_{EM} cells in T_{BP} CTs
180 are diffusely spread but with more concentrated toward the center of UMAP. This differential
181 distribution suggests that CT-matched cells express their respective signature genes more strongly
182 than T_{BP} clonotypes or those "CT-mismatched" cells (i.e., T_{CM} cells in T_{EM} CTs and T_{EM} cells in
183 T_{CM} CTs), thereby enhancing their fate determination. Consistent with this, RNA velocity analysis
184 supports the notion that T_{CM} and T_{EM} clonotypes represent more terminally differentiated states,
185 as directional flow arrows from CT-matched cells are either absent or pointed toward the outer
186 UMAP edges (Extended Data Fig. 3a). In contrast, T_{BP} clonotypes appear more interchangeable,
187 as the arrows from T_{CM} and T_{EM} cells in T_{BP} CTs indicate some bidirectional flow.
188
189 To determine whether the expression of all signature memory genes or only a specific
190 subset underlie the memory polarization, we analyzed differentially expressed genes in T_{EM} and
191 T_{CM} clusters (Supplementary Data 3) across CT-matched cells, CT-mismatched cells, and T_{CM} and
192 T_{EM} cells in T_{BP} CTs. Both aggregate T_{EM} and T_{CM} signature gene expressions increased
193 progressively with clonotype polarization (Extended Data Fig. 3b,c). Of the 126 T_{EM} signature
194 genes elevated in the T_{EM} cluster, only 45 genes, including *Ccl5*, *Gzmb*, *Gzmk*, and *Fasl* showed a
195 gradual increase in expression corresponding to the degree of clonotype polarization, suggesting
196 that these genes may contribute directly to clonotype fate commitment (Extended Data Fig. 3b).
197 Similarly, of 140 T_{CM} genes, only 65 genes, such as *Lef1*, *Tcf7*, and *Tnfsf8* exhibited graded
198 expression aligned with clonotype polarity, implying they are key regulators of T_{CM} fate (Extended
199 Data Fig. 3c).
200
201
202 **The T_{CM} repertoire is most variegated**

203 Having established that a TCR clonotype influences memory fate, we examined whether TCR
204 gene segment features are differentially associated with the T_{CM}, T_{EM}, and/or T_{BP} transcriptional
205 phenotype. V and J gene usage analysis revealed the preferences for TRAV16N/TRAV16, TRBJ2-
206 2/TRBJ2-7, and TRBV13-1 among all 242 NP-specific clonotypes (Fig. 2a), consistent with a
207 previous study [33]. Notably, the 140 T_{CM} clonotypes exhibited greater diversity in V and J gene
208 usage, while 44 T_{BP} clonotypes showed a more restricted repertoire, with a higher frequency of the
209 dominant VJ combinations found across the NP-specific TCRs. The 58 T_{EM} clonotypes displayed

210 an intermediate pattern. Entropy analysis confirmed the differences in VJ diversity among the
211 memory subsets (Extended Data Fig. 4a).

212 Next, we compared clonal burst sizes amongst memory populations. T_{CM} clonotypes were
213 the largest fraction in lower cell number categories, particularly in the single-cell group, compared
214 to T_{EM} clonotypes (Fig. 2b). In contrast, T_{BP} clonotypes were significantly more expanded than
215 either T_{CM} or T_{EM} clonotypes (Fig. 2c). Since clonotypes with only one cell cannot be classified as
216 T_{BP} by definition, we repeated the analysis excluding clonotypes with single-cell clonotypes and
217 observed consistent result (Extended Data Fig. 4b). These findings suggest that T_{CM} tend to persist
218 as a small number of cells, whereas T_{BP} are more clonally expanded.

219 To distinguish clonotypes with similar versus divergent TCR sequences, we categorized
220 branches of a TCR sequence tree into "short" and "long", respectively, based on paired TCR
221 sequence distances metrics (Fig. 2d). For each clonotype, we calculated the distance to all other
222 clonotypes and computed the mean of the top 10 shortest pairwise distances. For example, CT_25,
223 categorized as a short-branch clonotype, had a mean top 10 distance of 7.8, whereas CT_50,
224 categorized as a long-branch clonotype, had a corresponding value of 196.4 (Extended Data Fig.
225 5a,b). A histogram of these mean top 10 distances across all clonotypes revealed a bimodal
226 distribution, and we defined the valley between the two peaks (mean distance = 109) as the
227 threshold distinguishing short- and long-branch clonotypes (Extended Data Fig. 5b). A TCR
228 distance heatmap further supported the validity of this classification (Extended Data Fig. 5c).
229 Moreover, analysis of short- and long-branch clonotypes showed that short-branch clonotypes
230 exhibited more restricted V and J segments commonly used in NP-specific TCRs, whereas long-
231 branch clonotypes displayed greater diversity (Extended Data Fig. 5d).

232 We then examined DEGs between short vs. long branch clonotypes. Short-branch
233 clonotypes showed higher expression of T_{EM} genes such as *Gzmk* and *Ccl4*, whereas long-branch
234 clonotypes expressed higher levels of T_{CM} genes, including *Sell*, *Ccr7*, and *Satb1* (Fig. 2e and
235 Supplementary Data 4). Gene enrichment analysis confirmed a significant enrichment of T_{EM} gene
236 signatures in short branches and T_{CM} gene signatures in long branches (Fig. 2f). We further
237 examined the distribution of representative memory clonotypes on the TCR tree, including NP101
238 and NP105, identified from an independent scRNA-Seq experiment (Methods) with NP101
239 showing identical amino acid sequence to CT_5 and CT_56 (Supplementary Table 1) and NP105
240 bearing a significant relationship to NP204 described below. Representative T_{EM} clonotypes such
241 as NP201 and NP202, as well as T_{BP} clonotypes including NP34, NP63, NP101, NP206, and
242 NP207, fell within the short branch (Fig. 2d). In contrast, T_{CM} clonotypes NP41, NP204, and
243 NP205 were found in long branch, supporting the notion that TCR sequence similarity is associated
244 with T_{EM} or T_{BP} phenotypes, while greater sequence divergence is linked to the T_{CM} phenotype.

245 Deviations to this pattern include T_{CM} clonotypes NP105 and NP203 belonging to the short branch
246 (Fig. 2d). In the case of NP203, this is probably explained by the TCR sequence differing by only
247 1-3 amino acids from short-branch T_{BP} clonotypes NP101 and NP207 and T_{EM} clonotype NP202.
248 Hence, minor sequence differences can override the general pattern to influence fate decisions
249 despite overall amino acid similarity. This observation prompted us to pursue structural analyses
250 described in a later section to reveal "the exception that proves the rule". In sum, the T_{CM} repertoire

is more variegated than that of the T_{EM} repertoire but interclonal TCR distances *per se* do not define transcriptome polarity.

Weak TCR-$NP_{336-374}$/D^b bonding profiles

Single molecule (SM) TCRαβ-pMHC analysis was used to evaluate the performance and bonding characteristics of clonotypes belonging to each memory category (Extended Data Fig. 6a,b). T_{CM} clonotypes NP203, NP204, NP205, and NP105 were all weak binders with profiles consistent with slip-bonds. T_{EM} clonotypes NP202 and NP201 were also weak binders but exhibited more typical catch-bond profiles with peaks around 15 piconewtons (pN). T_{BP} clonotypes NP101 and NP207 exhibited mixed profiles, with higher lifetime amplitudes at both the typical slip and catch force regions (5 and 15 pN, respectively), while NP63 was a catch bond as in previous work[5]. Additionally, overall lifetime amplitudes were weak relative to verified digital clonotypes such as NP63[5] (Fig. 2g and Extended Data Fig. 6c). The ability to form a stable single-molecule TCRαβ-pMHC interaction irrespective of load was determined by comparing the total number of binding opportunities allowed to the total number of events measured. Stable tethering formation varied substantially among the clonotypes, with T_{CM} clonotypes showing a notably lower tendency to form stable bonds, which also tended to bind in the slip-type manner.

Excluding NP63, ranking relative performance based on lifetime amplitude around 15 pN in addition to the tendency to form stable tethers, suggest that T_{EM} clonotype NP202 and T_{BP} clonotypes NP207 and NP101 are a tier above T_{CM} clonotypes NP203, NP205, and NP105. NP204 and NP201 are the lowest performing clonotypes, exhibiting low lifetime amplitudes across all force ranges measured, coupled with a poor ability to form stable bonds measured by binding probability (Fig. 2h). Binding probability was strongest for NP202 (and NP63) compared to the other clonotypes profiled, where multiple tethers were observed.

Retrogenic profiling reprises polarization

To determine whether αβTCRs are linked to CD8 differentiative fate following antigen encounter and memory phenotypes identified by scRNA-seq reflect clonotype-specific polarization *in vivo*, we generated retrogenic chimera (RgC) mice. This was achieved by adoptively transferring naïve $CD8^+$ retrogenic (Rg) T cells from Rg donor mice into B6 [CD45 (2/2) Thy1.2] mice, followed by infection with the PR8 one day later (Fig. 2i). At 30dpi in mixed NP101/NP105 RgC mice, NP105 Rg T cells exhibited significantly higher expression of T_{CM} markers, CD62L and Tcf-1, compared to NP101 Rg T cells (Fig. 2j and Extended Data Fig. 7), indicating that the RgC system faithfully recapitulates clonotype polarization patterns identified by scRNA-seq.

Memory IAV crossreactivities

The role of T cells in providing heterosubtypic IAV protection to largely conserved epitopes is well established [34] despite limited structural analysis [35]. To ascertain if such crossreactivity could be extended more broadly to various memory clonotypes recognizing $NP_{366-374}$/D^b, we selected 16 TCRs that were transduced into mCD8αβ$^+$BW5147.3 (BW) cells and sorted for comparable TCR

294 expression. BW transductants were then stimulated with WT-PR8 $NP_{366-374}$ peptide or 9 naturally
295 occurring variant peptides derived from 11 other IAV strains [36] on APCs. IL-2 production was
296 assayed as a readout of TCR activation (Fig. 2k). The importance of the structurally featured
297 residues of the peptide (p4E, p6M and p7E) were also quantified (Extended Data Fig. 8a,b) and
298 referenced to the IAV variants (Extended Data Fig. 8c). Crossreactivity was observed in 14 of 16
299 TCRs, ranging from 1-6 of the 9 variants, with all TCRs responding to the isologous PR8 strain
300 (Fig. 2k and Extended Data Fig. 8b,d). As 0/6 T_{EM}, 1/5 T_{CM} and 3/5 T_{BP} recognized 5 or more viral
301 epitopes, T_{BP} recognition trended as more crossreactive compared to the polar clonotypes ($p =$
302 0.0632 using a two-tailed Fisher's exact test). The greatest crossreactivity was exclusive to the T_{BP}
303 (NP101, NP206 and NP207). As an example, detailed IL-2 production from NP207 is further
304 quantified by peptide titration (Extended Data Fig. 8e).

305

306 **Protein expression, crystallization, and analyses**

307

308 To obtain diffraction quality crystals of TCRαβ-$NP_{366-374}/D^b$ complexes for structural studies, we
309 engineered mouse TCRs and TCR chimeras with murine V domains fused to human C domains
310 (sequences in Supplementary Data 5). All TCRαβ heterodimers were generated in eukaryotic
311 Expi293F N-acetylglucoseaminotransferase I-deficient ($GnTI^-$) cells to facilitate deglycosylation
312 under native conditions. H-$2D^b$ and β2m proteins were produced in *E. coli* and refolded *in vitro*
313 with chemically synthesized $NP_{336-374}$ peptide to generate pMHC complexes. Procedures for
314 purifications, crystallization screening, and data collection are detailed in Methods. A series of
315 crystals of unligated TCRs and their complexes were obtained and structurally determined.
316 Crystallographic statistics, complex interface buried surface areas (BSA) and surface
317 complementarity (Sc values) along with H-bonding and van der Waals interactions are given in
318 Supplementary Table 2-4. Supplementary Discussion Item 1-4 offer specific information on
319 TCRαβ apoproteins, both wild-type (wt) and chimeras, and delineate incidence, twist, and shift
320 docking parameters on the same $NP_{336-374}/D^b$ ligand.

321

322 Fig. 3a tabulates information on the six TCRs from B6 mice that recognize the $NP_{366-374}$
323 PR8 IAV epitope used for structural analysis. Four TCRs are representative of T_{EM} (NP202), T_{BP}
324 (NP101, NP207), and T_{CM} (NP203). It is striking that the TCRs utilize identical TRAV and TRBV
325 gene segments differing by only 1-3 CDR3 amino acid residues and yet belong to functionally
326 distinct memory CD8 subsets (Fig. 3a). We also selected the NP204 and NP105 T_{CM} TCRs
327 comprising distinct V gene segments but with similar CDR3β loops given a shared TRBJ1-6
328 differing but just 4 of 17 residues. Note that CT_29 (Supplementary Table 1) is a T_{CM} like NP105
329 and NP204. CT_29 is most similar to NP105 with utilization of the same TRAV, TRBV, TRBJ,
330 but a different TRAJ.

331

332 Each of the six TCRs adopts a canonical binding mode in their respective complex such
333 that Vβ overlies the C-terminal half of the peptide and the MHC α1 helix while Vα overlies the
334 N-terminal half of the peptide and MHCα2 (Fig. 3b). Amongst the various TCR-$NP_{336-374}/D^b$
335 complexes, the docking modes of the four closely related clonotypes, NP202, NP101, NP207 and
336 NP203 appear quite similar and with comparable footprints on $NP_{366-374}/D^b$ (Fig. 3c), complex
337 interfaces (BSA and Sc) (Supplementary Table 3), and docking parameters (incidence angle, twist
338 and shift) (Supplementary Discussion Item 4). Those interactions are certainly distinct from the

339 two footprints of the "Vβ-centric" NP105 and NP204 TCRs analyzed using the same set of
340 parameters. We refer to NP105 and NP204 as Vβ-centric since the TCR-pMHC complex in each
341 is dominated by structural interactions involving its Vβ domain. For these two Vβ centric TCRs,
342 the ratio of TCRα/TCRβ BSA in the TCR-pMHC complex is 0.26-0.59. In contrast, for the four
343 NP 202, NP101, NP207 and NP203, these parameters are 1.23-1.33, due to considerably greater
344 Vα interactions. Amongst those four highly related NP TCRs, their distinct interactions with NP_{336-}
345 $_{374}/D^b$ are only appreciated following detailed structural examination.
346
347
348 **Atomistic basis of CD8 memory fates**
349
350 The primary crystallographic features of the NP202 T_{EM} TCR clonotype's interaction with NP_{336-}
351 $_{374}/D^b$ are shared with NP101, NP207 and NP203 interactions. The most exposed $NP_{336-374}$ peptide
352 residues extending upward from the MHC groove are p4E and p6M, and to a lesser extent, p8T
353 (Extended Data Fig. 8a), in agreement with a prior pMHC structure [37]. When the NP202 TCR
354 docks on $NP_{366-374}/D^b$, the negatively charged carboxylic group of p4E is positioned below the
355 center of a glycine-rich loop from CDR3α, forming 2-3 H-bonds to the amide groups (Fig. 3d).
356 The central p6M sidechain is sandwiched by CDR3α and CDR3β and constrained in a
357 hydrophobic pocket involving aliphatic sidechains of K98α and R99β. An additional specific
358 interaction is a H-bond between side chains of p3N and CDR3 K98α.
359
360 The NP101 T_{BP} TCR differs from the NP202 T_{EM} TCR by a single CDR3β residue (D95β
361 vs. E95β), as highlighted in Fig. 4a. Consequently, the two TCR docking angles and binding sites
362 on $NP_{366-374}/D^b$ are very similar (Supplementary Discussion Item 4). Structural alignment of their
363 H-$2D^b$ α1α2 domains demonstrates excellent overlay of the peptide binding grooves and
364 corresponding $NP_{366-374}$ peptides except at the central p6M residue differing by a slight shift and
365 side chain rotation. Although the single-residue substitution resides in CDR3β, the Vβ domain
366 including CDR3β exhibit limited deviation (shortest red arrow). However, a positional shift is
367 evident in the Vα domain comparison as a combined result of slightly different TCR docking
368 angles onto the pMHC and deviations at the Vα-Vβ interface between the two TCR V modules
369 (longer two red arrows). This shift brings important pocket-forming residues, including F33α and
370 Y54α (in green), as well as the aliphatic part of R99β (in cyan), closer to p6M, which significantly
371 reduces the size of the hydrophobic pocket. For example, the Cα-Cα distance between D52α and
372 R99β, a representative distance between CDR2α and CDR3β, is reduced from 7.78Å in NP202 to
373 6.80Å in NP101. The apposition of the Vα C' strand edge of to the Vβ G strand edge is reflected
374 in the formation of two salt bridges, R50α to E101β and D52α to R99β in NP101. Shrinking of
375 the p6M hydrophobic pocket strengthens hydrophobic and van der Waals interactions with NP101.
376 Meanwhile, the distant interaction between p4E to G100α is lost in NP101 (Supplementary Table
377 4). Together, the overall structural alterations foster the repositioning of the TCR-pMHC
378 interaction center from the p4E to the p6M residue, thereby doubling the number of p6M van der
379 Waals contacts made by NP101 relative to NP202 (3 vs 6, Supplementary Table 4). This subtle
380 difference is not revealed by TCR docking angles or footprints onto pMHC (Supplementary
381 Discussion Item 4 or Fig. 3c). A second T_{BP} clonotype, namely NP207, manifests a similar shift
382 akin to NP101 associated with TCR crossreactivity against variant $NP_{366-374}$ heterotypic IAV
383 strains, as noted in Fig. 2k and Extended Data Fig. 8.

NP207 (T_{BP}) and NP203 (T_{CM}) differ at two residues, K98α vs R98α in CDR3α and V99β vs L99β in CDR3β, respectively, as highlighted in Fig. 4b. In the NP207-$NP_{366-374}/D^b$ complex, K98α forms a H-bond with p3N. A well-defined water molecule (labeled as W) also bridges the interactions between K98α and p3N to the ND1 atom of H155 in the D^b α2-helix. Meanwhile, p7E and NE2 of H155 form a salt bridge. However, in the NP203 complex, the longer R98α sidechain both pushes p3N slightly downward and displaces the water molecule found in the NP207 complex to form a salt bridge directly with the ND1 atom of H155. The ND1 atom of H155 is likely deprotonated to neutralize the extra positive charge introduced by the K→R substitution, while the NE2 of H155 is protonated and neutralized by p7E, thereby becoming indispensable in the NP203 TCR recognition of pMHC, in contrast to NP207, as elaborated below. The CDR3β L99 in NP203 (T_{CM}) relative to CDR3β V94 in NP207 (T_{BP}) augments van der Waals contacts with p6M, whereas the H-bonds of p4E to CDR3α are weakened with the bond length (p4E to G101α) increase from 2.97Å to 3.34Å (Supplementary Table 4). These changes collectively contribute to the apparent shift of the NP203 TCR mechanical load from α chain to β chain.

Fig. 4c reveals two additional differences between the NP207 (T_{BP}) and NP203 (T_{CM}) complexes related to their respective Vα domains and the single N-glycosylation site adduct. In NP207, as well as in NP101 and NP202, the Vα C" edge strand of shifts from the GFCC' to the ABED face as commonly observed in TCR Vα domains [38]. In NP207, the conserved N-glycan binding residue N58α is a part of CDR2α. The first N-acetylglucosamine (GlcNAc) attached to N58α is visible in the structure, pointing away from the ABEDC" sheet of Vα domain. In this orientation, even a mature N-linked glycan attached to N58α is unlikely to extend to the TCR-pMHC interface. In contrast, in the NP203 complex, the C" of Vα domain is absent with no secondary structural element between C'-strand and D-strand. Instead, the extended loop from C'- to D-strands is stabilized by two side chain-main chain H-bonds between the loop and the D-strand (boxed insert in Fig. 4c). Because E57α points to the D-strand, N58α pivots from the D-strand to the interface edge between the Vα C'-stand and the Vβ G-strand, repositioning the attached GlcNAc to above the α2-helix apex. The N-glycan with its additional sugar adducts attached to N58α (absent here due to EndoH cleavage) presumably contacts the pMHC, impacting TCR ligation, mechanotransduction involving the TCR-pMHC interface, and NP203 T_{CM} polarity.

Considering the striking divergence in the transcriptomes of the NP202, NP101, NP207 and NP203 clonotypes, these structural distinctions must impact gene activation. Molecular dynamics simulations under force show that interdomain motion, molecular compliance, fluctuating forces, and interfacial contacts collectively determine the mechanical response and fine peptide TCR discrimination [39,40]. To measure differential physical stress responses of individual clonotypes we counted the number of TCRα and TCRβ residues that form 6 or more intradomain contacts with occupancy greater than 80% during a 700ns simulation. The greater the number of these 'hub' residues, the more tightly packed and rigid the corresponding domain is, which indicates that the domain bears greater physical load. Although these TCRs differ by only a few amino acids (Fig. 3a), under identical loading conditions the numbers of the hub residues varied considerably among the 4 subdomains (Supplementary Discussion Item 5), which comports with exquisite biomechanical nuancing.

429
430 The two NP204 and NP105 T_{CM} clonotypes distinguish themselves from NP202, NP101,
431 NP207 and NP203 above by their Vβ-dominant docking footprints on $NP_{336-374}/D^b$ (Fig. 3b,c), and
432 as further visualized by the comparison of NP202 versus NP105 side views (Fig. 4d, left panel).
433 The NP105 TCR-pMHC interaction is dominated by Vβ, notably involving its
434 CDR3β motif D96RRxS100β (Fig. 4d, right panel). The NP105 CDR3β D96 forms a hydrogen
435 bond to p8T, akin to D95β or E95β found in other NP TCRs. Meanwhile, R97β forms a salt bridge
436 to p4E, which lacks interaction with the Vα domain in contrast to the four TRBV5-containing NP
437 TCRs (Fig. 4a,b). R98β forms a H-bond to the carbonyl group of p5N. The side chain and amide
438 group of S100β form a pair of H-bonds with the p7E sidechain. Furthermore, p6M is no longer
439 sandwiched between Vα and Vβ. Instead, it is surrounded by a part of CDR3β (from R98β to
440 S100β) and MHC residues H155 and Y156 (not shown) and capped by Y94α of CDR3α.
441 Strikingly, the Vα contribution to peptide recognition is minimal. The primary features of the Vβ-
442 dominant docking in NP105 are largely conserved in the other T_{CM} NP204 that utilizes distinct Vα
443 and Vβ genes but shares the CDR3β motif with NP105 (Extended Data Fig. 8g).
444
445 **Differential tyrosine phosphorylation and V-centric TCR binding**
446
447 The distinct transcriptional programs elicited by pMHC ligation of TCRs, correlating with Vα- vs
448 Vβ-centric interactions , suggest that different downstream signaling pathways should be apparent,
449 especially considering the known compartmentalization of CD3 dimers in the holoreceptor
450 (Extended Data Fig. 9a,b). As CD3ζ tyrosine phosphorylation is maximal at 1 minute following
451 pMHC ligation of TCRs in triggered T cells[41], we used this as a proxy to investigate NP202 versus
452 NP105. As shown in Extended Data Fig. 9c, the NP202-associated CD3ζ subunit is significantly
453 more phosphorylated following $NP_{366-374}/D^b$ tetramer stimulation compared to that of NP105, as
454 measured by phospho-Tyr 142 detection. This difference in three independent experiments is not
455 due to reduced NP105 signaling ability, as higher molecular weight proteins in the 50-75 kDa and
456 100-120 kDa ranges are as or more heavily phosphorylated in NP105 compared to NP202
457 (Extended Data Fig. 9d). Yet, within the ~20-25 kDa range, where the CD3 subunits are found to
458 migrate, the NP202 appears to result in a greater level of phosphorylation. Thus, while the NP202
459 α-dominant TCR results in higher levels of CD3 phosphorylation, the NP105 β-dominant TCR
460 shows phosphorylation of alternative signaling proteins.
461
462 **Structural basis of heterosubtypic immunity**
463
464 Structural analysis also delineates the basis for differential TCR heterosubtypic immunity. For
465 example, NP105 tolerates a peptide E7D viral mutation, whereas NP204 does not. The weaker H-
466 bonds between pE7 and CDR3β residues in NP204 (approximated as 3.10 Å and 3.49 Å) would
467 have a greater impact than those between pE7 and CDR3β residues in NP105, which are shorter
468 (2.77 Å and 2.82 Å) (Supplementary Table 4). Pointedly, the E7D mutation results in a 1.54Å
469 sidechain foreshortening given a loss of one carbon-carbon bond. Distances between hydrogen
470 bonding atoms would likely become too weak and break for NP204. Likewise, the tilt observed in
471 NP101 (Fig. 4a) and NP207 (Extended Data Fig. 8f) relative to the T_{EM} NP202, makes both T_{BP}
472 clonotypes more crossreactive to p6M variants given that smaller sidechains such as I, L and V

(Fig 2k) readily accommodate the reduction in volume of the hydrophobic pocket hosting the central p6 residue.

Activated T_{CM} performance

Because high numbers of transferred T cells modulate memory phenotypes during antigen competition [16-18], we asked whether TCRs would continue to dictate intrinsic differentiation bias under such challenging conditions. 100,000 Rg T cells bearing NP101 or NP105 TCRs were adoptively transferred to B6 hosts and infected with PR8 24 hrs later. Then, at 35 dpi mLNs were isolated and Rg T cells were sorted based on congenic markers. PCA of gene expression following RNA-Seq for the 14 individual lymph node samples (7 for NP101 [C101 series], 7 for NP105 [C105 series]) delineated 3 clusters, 2 consisting only of NP101 (Cluster 1) or NP105 (Cluster 3), and an intermediate cluster (Cluster 2) of mixed clonotypes (Fig. 5a). Differential expression of the top 500 genes identified 2 clear sets of genes partitioning with high probability between the NP101 and NP105 clusters (Fig. 5b). Manual curation of the gene list for those reported to have T cell functionality reduced the set to 59 expressed genes segregating with high probability between the NP101 cluster and the NP105 cluster (Fig. 5c). Application of this gene list to all 3 clusters identified the NP101 cluster 1 as displaying an exhaustion signature, as generally found in T_{EM}, especially in chronic infection and tumor environments [42,43]. In contrast, the NP105 cluster expressing higher *Sell, Il7r* and *Bcl2* transcripts together with cytotoxic transcripts (*Gzma/Gzmb)* and active metabolic programming (*Myc*) as well as stem cell proliferative genes (*Placd8, Pim1*) suggested an activated T_{CM} state with effector functionality (Fig. 5d). Meanwhile, Cluster 2 with mixed NP101/NP105 samples revealed a representation of both activated T_{CM} and exhaustion signatures. To extend these findings, we performed a similar independent RNA-Seq for NP202, NP204, and NP207 Rg T cells (C202/C204/C207 series). Clustering of this dataset revealed a graded activation signature in addition to the T_{CM} and exhaustion signature (Extended Data Fig. 10). Aggregation of the data (Extended Data Fig. 10e) identified differential partitioning by cluster of the clonotypic retrogenic cells implying this was a property of each unique NP-specific TCR (Fig. 5e). By χ^2 analysis, C101 and C105 samples partition differentially between clusters 1-3 ($\chi^2 = 19.14$, dof = 6, $P < 0.004$), and the C202, C204, and C207 dataset also partition differentially between clusters 1-4 ($\chi^2 = 23.33$, dof = 9, $P < 0.006$). Notably, only NP105 and NP204 manifest as activated T_{CM}. Collectively, the deep bulk RNA-seq analyses identified TCR-linked CD8 IAV memory responses of adoptively transferred Rg T cells to manifest greater exhaustion of T_{BP} and T_{EM} counterparts relative to that of T_{CM} under adverse conditions.

Discussion

TCR-pMHC interaction *per se,* primarily dictates fate commitment as revealed through single cell transcriptomic/paired TCR analysis of B6 mice as well as TCR retrogenic chimeric animals. While clonal plasticity, as noted herein (Fig. 5 and Extended Data Fig. 10) and reported elsewhere [44], exists in relation to T-cell functionality states responsive to environmental queuing, TCR-linked transcriptome bias is unquestionable. In this context, *Abdullah et al.* [44] recently explored recombinant vesicular stomatitis virus (VSV), as well as the more inflammatory bacterial *Listeria monocytogenes* systems, to study the naive SIINFEKL/K^b T cell response during those infections.

For both systems, TCR intrinsic bias among clonotypes was observed by day 7 of the acute response, when short-lived effectors and memory precursor effector CD8 T-cells were generated, several weeks in advance of memory development. Given that Abdullah *et al.* and our current study utilized different pathogens and kinetics to affirm that TCR-pMHC interaction is critical for naïve CD8 T cell differentiation, the collective conclusions are broad and complementary.

The structural mechanisms underlying fate determination were identified here through structural analyses of six distinct TCR-$NP_{366-374}/D^b$ complexes. Two tiers of differential interactions were observed. In the first tier, a pronounced positional docking variance as to TCR footprints of Vα versus Vβ domains, as well as BSA of each's TCR-pMHC interaction, pointed to differential binding of T_{EM} and T_{CM} for NP202 vs NP105 and NP204, respectively. The former TCR was dominated by Vα interactions focused over the α1 MHC helix, whereas the latter two TCRs were Vβ binding centered around the α2 MHC helix. In these examples, the distinct TCR footprint topologies at the ligand interface are termed Vα-centric for NP202 and Vβ-centric for NP105 and NP204. Within the αβTCR holoreceptor complex, eight of the 10 cytoplasmic tail ITAMs (CD3εδ, CD3ζζ) are attached to the inner leaflet of the membrane on the TCRα side, but just 2 (CD3εγ) are located on the TCRβ side and further compartmentalized by transmembrane segments separated by intercalated cholesterol molecules [[45] and references therein] (Extended Data Fig. 9b). Such partitioning and binding asymmetry likely foster divergent signaling following ITAM release (reviewed in [31]), impacting the magnitude and quality of downstream responses as reflected in differential gene signatures noted after one week [44] and one month (current study), and is consistent with the differential tyrosine phosphorylation observed herein for CD3ζζ. Signaling differences probably also relate to the greater memory expansion mediated by the T_{BP} clonotypes.

As the preTCR lacks a Vα domain in its pTα surrogate subunit that pairs with a canonical β subunit preceding αβTCR development in the thymus [46], we posit that the preTCR pTα-β heterodimer is an extreme example of a Vβ-centric interaction linked to asymmetric mechanotransduction [47-49]. Given that the preTCR functions to foster survival [50], promoting the incorporation and persistence of β chains into the evolving αβ lineage of thymocytes, there is an analogy to Vβ-centricity involving peripheral T cells associated with long-term T_{CM} development and renewal, i.e. stemness. Consistent with this notion, five key genes involved in transcriptional programming and/or survival that are upregulated in common during the preTCR-dependent β-selection checkpoint and CD8 T_{CM} memory generation are *Tcf7* [7,51], *Lef1* [8,51], *Il7r* [52,53], *Id3* [9,54] and *Bcl2* [55,56]. By contrast, T_{EM} promote rapid effector functions but generally displays more limited survival and cellular plasticity characteristics [1-3].

In the second tier of docking interactions, there is pronounced subtlety as footprints of NP202, NP101, NP207 and NP203 are largely indistinguishable. Nonetheless, NP203 is less capable of transducing TCRα-associated signals for two reasons: first, Vα structural rigidity is attenuated by loss of the NP203 C" strand, and second, the attendant glycan adduct intercalating between TCR and pMHC interaction surfaces may dampen applied physical load. We postulate that this diminished TCRα mechanotransduction fosters T_{CM} development. In contrast, NP101 and NP207 T_{BP} TCRs are without such structural impediments, but both are tilted to the Vβ side relative to NP202 T_{EM}. We posit that tilt results in a differential force vector to transmit load, creating a more comparable Vα/Vβ balance centered on the smaller TCR pocket hosting p6M,

fostering T_{BP} development unlike that of the more Vα dominant NP202 programming T_{EM} differentiation.

Fig. 6 provides an overview of our observations. Panel a shows that CD3 signaling molecules are asymmetrically positioned relative to the TCRα and TCRβ subunits, while panel b illustrates that antigenic peptide residues and MHC helices interact in various patterns at the TCR-pMHC interface, demonstrated by comparison of NP202, NP207, and NP105 as examples. Panel c uses a seesaw analogy to explain how mechanical forces are transmitted through the TCR subunits with ball size representing the relative mechanical load from the pMHC. Just as gravity tilts a seesaw, uneven loading on the TCR influences which signaling pathways are activated. When the load is balanced, i.e. for T_{BP} clonotypes, it allows for stochastic outcomes in how T cells differentiate into T_{EM} or T_{CM} progeny during repeated cycles of attachment and detachment from antigen-presenting cells (APCs) throughout clonal expansion [57-59] This balanced distribution of T_{EM} and T_{CM} likely results from chance mechanical interactions at the contact points between T cell microvilli and APCs, which generate different shear forces. In contrast, when the load is biased, as regards polar T_{EM} and T_{CM} clonotypes, impact from this randomness is reduced and the T cell is more likely to follow a specific signaling pathway.

Shrewdness in TCR mechanotransduction biology can dictate digital vs analog TCR performance based on as little as a single CDR3α amino acid variation among two TCRs (NP63 vs. NP34) binding to the same $NP_{366-374}/D^b$ ligand [5]. Conversely, a single amino acid change in a peptide ligand (i.e , APL) bound to one MHC molecule can generate differential functional T cell activation through the same TCR [60]. For the latter, molecular dynamics simulations under force revealed a combined role of interdomain motion, molecular compliance, fluctuating forces, and interfacial contacts that collectively determine the mechanical response and fine peptide TCR discrimination [39,40]. The differential physical stress response observed here by molecular dynamics amongst closely related TCRαβ sequences underscores this exquisite nuancing (Supplementary Discussion Item 5).

Given different clonotypic TCR sequences comprising a single T-cell repertoire, those TCRs may experience varying levels of stress and strain distributions upon mechanical loading. Thus, their load propagation pathways through the ectodomains of the αβTCR holoreceptor into the membrane and cytoplasmic tail elements may also deviate. These differences (Extended Data Fig. 9) likely instruct distinguishable release of the ten ITAMs per αβTCR complex and engage divergent downstream signaling, comporting with our distinct tyrosine phosphorylation data and transcriptomes. It is important to highlight that bipolar (balanced) vs polar (unbalanced) signaling is evident for G-protein coupled receptors (GPCRs), where activating both G-protein and β-arrestin routes collectively versus the latter alone dramatically alters functional cellular outcome in μ-opioid and chemokine receptors (reviewed in [61]). For GPCRs, however, dissimilar ligands acting on the same receptors mediate the differential outcomes, whereas in the T-cell memory system explored here, the TCRs are distinct receptors that bind the same pMHC. While nearly all of the ~800 various GPCRs are not mechanosensors, unlike TCRs, our findings hold significant biological relevance and, as noted, are not without precedence[62 63].

The $NP_{366-374}/D^b$ T-cell repertoire is generated against a ligand expressed at ~2000 copies/antigen-presenting cell [64] utilizing mostly analog TCRs [5]. The crossreactivities found in

606 ~20% of the TCRs offer a teleological explanation for the highly divergent TCRs incorporated into
607 the memory niche, namely to foster recognition of natural viral strain diversification. The T_{BP}
608 clonotypes in our analysis manifest the greatest crossreactivity and largest burst sizes with rapid
609 cytotoxicity derived from their T_{EM} progeny, implying superior attributes. However, the T_{CM}
610 revealed the least exhaustion and greatest TCR repertoire diversity comprising single-cell
611 clonotypes occupying compact memory niche "real estate" to recognize viral variants. We predict
612 that a comparable memory niche strategy is also found in other CD8 repertoires, including PA_{224-}
613 $_{233}/D^b$, where digital performers are elicited exclusively due to the sparseness of antigen display [5]
614 and shall extend to CD4 repertoires directed at pMHC class II epitopes as well. Harnessing this
615 multidimensional information presents a compelling opportunity to create immunotherapies
616 involving both TCR and synthetic receptor designs, incorporating necessary survival and persistent
617 effector functionalities. Consideration of receptor-pMHC binding centricities can likely improve
618 upon clever AI-based designs [65-67] or other cellular therapies to foster effective clinical translation.
619
620

621 **Methods**
622
623 **Mice and IAV infection**
624
625 C57BL/6N (B6), B6.129S6-Rag2^{tm1Fwa}N12 (*Rag2*$^{-/-}$), and B6.SJL-*Ptprc*^{a}/BoyAiTac (CD45.1/1)
626 mice were purchased from Taconic Biosciences, Inc. B6.PL-*Thy1*^{a}/CyJ (Thy1.1) were obtained
627 from The Jackson Laboratory. CD45.1/1-*Rag2*$^{-/-}$ and CD45.1/2-*Rag2*$^{-/-}$ were generated by
628 intercrossing CD45.1/1 and *Rag2*$^{-/-}$ strains. Thy1.1-*Rag2*$^{-/-}$ mice were generated by intercrossing
629 Thy1.1 and *Rag2*$^{-/-}$ mice. All mice were housed and bred under specific pathogen-free conditions
630 at the Dana-Farber Cancer Institute (DFCI) Animal Facility, accredited by the Association for
631 Assessment and Accreditation of Laboratory Animal Care (AAALAC). Euthanasia was performed
632 by CO_2 inhalation followed by cervical dislocation. Mice aged 6-10 weeks were used for
633 experiments. Sex-matched mice were used for each experiment. No gender preference was applied,
634 and the sex in each experiment was not deliberately selected.
635 Mice were infected intranasally with 20 EID_{50} of Influenza A/PR/8/34 virus (PR8, H1N1, Charles
636 River Laboratories) as a primary infection under anesthesia with intraperitoneal injection of
637 ketamine/xylazine (120 mg/kg ketamine, 10 mg/kg xylazine) PR8-infected mice were
638 rechallenged intranasally with $1x10^7$ EID_{50} of serologically distinct X:31, A/Aichi/68 (X31, H3N2,
639 Charles River Laboratories). These viral doses were used consistently across all experiments. All
640 mouse maintenance, breeding, and experimental procedures were approved under Dana-Farber
641 Cancer Institute Institutional Animal Care and Use Committee (IACUC) protocol 04-113.
642
643
644 **Cell lines and cell culture**
645
646 BW5147.3 cells and CD3δγεζ pMIY vector were a gift from the Vignali lab (St. Jude Children's
647 Research Hospital, Memphis, Tennessee), and mCD8$\alpha\beta^+$ BW5147.3 cells were generated as
648 previously described [22]. The cells were maintained in D10 [DMEM medium (Gibco), 10% fetal
649 bovine serum (FBS) (Sigma-Aldrich), 100 IU Penicillin and 100μg/mL Streptomycin (Corning),
650 2 mM L-glutamine (Corning) and 55 μM 2-mercaptoethanol (Gibco)] with 400 μg/mL
651 Hygromycin B (Gibco) and 400 μg/mL Geneticin (Gibco). R8 cells were maintained in R10
652 (RPMI-1640 (Gibco), 10% FBS, 100 IU Penicillin and 100 μg/mL Streptomycin, and 55 μM 2-
653 mercaptoethanol). All cells were grown in a 5% CO_2 incubator at 37°C.
654
655
656 **Cell isolation, flow cytometry and cell sorting**
657
658 Mediastinal lymph nodes (mLNs) were harvested, mashed with a 3 mL syringe on a 24-well plate
659 with RPMI-1640, filtered with 80 μm mesh, washed with RPMI-1640, and resuspended with
660 FACS buffer (2% FBS/0.05% NaN_3/PBS) or appropriate buffer as indicated for the following
661 experiments. Cell suspensions from mLN were first treated with anti-mouse CD16/CD32 mAbs in
662 FACS buffer to block FcR binding for 10 minutes at 4°C and then stained with antibodies indicated
663 in each figure caption in FACS buffer for 20 minutes at 4°C. For intracellular staining, cells were
664 fixed with 4% PFA/PBS and permeabilized using permeabilization buffer following the
665 manufacturer's protocol (Invitrogen). After washing, cells were incubated with anti-mouse TCF-1
666 mAb for 30 minutes at 4 °C. For scRNA-seq of $NP_{366-374}$ /H-2D^b-specific memory T cells, cell

suspensions from pooled mLNs from 10 mice was stained with APC-conjugated $NP_{366-374}$ /H-2D^b tetramer (MBL International Corporation) for 30 min at RT followed by staining with Zombie Aqua, and CD8β and CD44 mAb. $NP_{366-374}$-tetramer$^+$ cells were sorted after gating on Zombie Aqua$^-$ CD8β$^+$ CD44$^+$ cells. For scRNA-seq of non-tetramer sorted T cells at memory and recall phase, Zombie Aqua$^-$ CD8b$^+$ and CD44$^+$ cells were sorted from pooled mLNs from four and two mice, respectively. Rg T cells for bulk RNA-Seq were isolated from individual RgC mouse mLN as Zombie$^-$ CD8β$^+$ cells in combination with congenic markers CD45.1, CD45.2, and Thy1.1. All antibodies and the concentration used are listed in Supplementary Data 6. All cells were analyzed on a BD LSR Fortessa™ Cell Analyzer (BD Biosciences) or sorted on a FACS Aria II (BD Biosciences). Data were analyzed with FlowJo software (FlowJo, LLC).

Single-cell RNASeq library construction and sequencing

$NP_{366-374}$-specific memory CD8$^+$ cells were sorted into 500 mL R10 in 1.5 mL tube. Cell density was adjusted to analyze 10,000 cells per sample. Single-cell gene expression (scRNA-seq) was performed using Chromium Single Cell 5' Library and Gel Bead Kit with V(D)J enrichment kit (10x Genomics). Gel Bead-in-Emulsion reverse transcription (GEM-RT) reaction, clean-up, and PCR amplification were performed to obtain cDNA for library generation. Single cell sequencing libraries were generated using 5'GEM-X v1 according to manufacturer's protocol. Libraries were uniquely indexed for multiplexed sequencing. Libraries were single i7-indexed using the Chromium i7 Multiplex kit (indices listed in table). Following isolation and clean-up of library DNA, concentration and fragment size were assessed using an Agilent Bioanalyzer and quantification by Qubit analysis (ThermoFisher). 150bp paired-end sequencing was performed on a Hiseq 3000 utilizing the following allocation parameters per lane: two 5'GEM-X libraries (2 x 40% of reads) and two V(D)J libraries (2 x 10% of reads).

Single-cell RNA-seq data analysis

Gene expression and TCR FASTQ files were processed using CellRanger version 3.1.0 [68] using the GRCm38 mouse genome reference. The R package Seurat (version 5.1.0) [69] was used to filter out cells, cluster the data using 7 principal components, and perform downstream analyses. Cells were required to have less than 10% of mitochondrial content, between 5 and 7,000 features, and a minimum of 1,000 UMIs. Potential doublets were removed using the Python package "scrublet" with default parameters [70]. Additionally, only those cell with exactly one alpha TCR chain and exactly one beta TCR chain were retained. Gene signature scores were calculated using the package AUCell (version 1.26) [71]. The first principal component was used to generate a cell density ridge plot. UMAP approach was used for data visualization [72].

Verification of memory clusters

scRNA-seq was performed on non-tetramer sorted (NS) memory CD8 T cells from mLNs, and these were processed as described above with cluster resolution set to "0.2". Previously defined gene sets associated with T_{CM} and T_{EM} cells [73] and AUCell were used to determine which clusters

713 in the NS data constituted T_{CM} and T_{EM} clusters. Differential gene expression between NS T_{EM}
714 clusters and T_{CM} clusters was performed using "FindMarkers" from the "Seurat" package with
715 "min.pct" set to 0.3. Final T_{EM} and T_{CM} signatures were those with an adjusted p-value <= 0.05,
716 and, for T_{EM}, (pct.1 – pct.2) >= 0.3 and pct.2 < 0.2 and, for T_{CM}, (pct.1 – pct.2) <= -0.3 and pct.1
717 < 0.2. The final T_{EM} gene signature includes *"Gzmk", "Itga1", "S100a4", "Id2", "S100a6", "Mdfic",*
718 *"Rgs1", "Fasl", "Pdcd1", "Ly6a",* and *"AU020206*". The final T_{CM} gene signature includes *"Sell",*
719 *"Satb1", "Tmem108", "Txk", "Nsg2", "S1pr1", "Cmah", "Pde2a", "Ccr7", "Treml2", "Rras2",*
720 *"Dapl1", "Il6st", "Pdlim1", "Id3",* and *"Dennd2d"*. These gene signatures were used to verify T_{CM}
721 and T_{EM} clusters on scRNA-seq of $NP_{366-374}/D^b$-specific memory CD8 T cells using "AUCell".
722
723
724 **Memory clonotype definition**
725
726 T_{CM} and T_{EM} clonotypes were broadly defined as those in which more than 70% of cells localized
727 to the polarized T_{CM} or T_{EM} cluster, respectively. T_{BP} clonotypes were those in which fewer than
728 70% of cells localized to either cluster. Polarized clonotypes manifest statistically distinct and non-
729 random distributions in contrast to bipolar clonotypes.
730
731
732 **Clonotype origin**
733
734 Clonotypes NP201-207 were isolated from pooled mLNs of 10 B6 mice at day 34 following
735 primary infection with the PR8 strain of IAV. Clonotypes NP101 and NP105 were derived from
736 pooled mLNs of 2 B6 mice undergoing a memory recall response, 4 days after heterologous
737 challenge with X31. Clonotypes NP34, NP41, and NP63 were previously identified from lungs 5
738 days after secondary X31 infection [5]. Clonotypes NP1-3 were isolated from the T_{EM} cluster of
739 $CD44^+$ memory $CD8\beta^+$ T cells sorted from pooled mLNs of four B6 mice at day 33 post-infection.
740
741
742 **Gene enrichment analysis**
743
744 Gene Set Enrichment analysis was performed on $\log_2$ fold changes using the "GSEA" function of
745 the R package "clusterProfiler" (version 4.12.6) [74] with parameters minGSSize = 6 and
746 pAdjustMethod = "fdr".
747
748
749 **RNA velocity analysis**
750
751 Intronic read counts were calculated using "velocyto" (version 0.17.17) [75]. The Python package
752 "scVelo" (version 0.2.5) [76] was used to perform velocity analysis using parameter mode set to
753 'stochastic'.
754
755
756 **Generation of TCR sequence tree and analysis**
757 Va and Vb sequence similarities (TCR distances) were calculated using the package "TCRDist3"
758 (version 0.2.2) [77] with the distance matrices for the two summed. Clonotypes with the TRBV gene

"TRBV12-2+TRBV13-2" were excluded from the analysis due to the absence of this V-gene from the TCRDist3 database. A distance cladogram was generated using the R package "hclust" using complete linkage. The R package "pheatmap" (version 1.0.12) was used to create a heatmap of TCR distances.

Definition of short and long branch

Short and long branches of the TCR tree are defined based on pairwise TCR sequence distance metrics. First, the mean of the top 10 shortest pairwise distances was calculated for each clonotype. Then the threshold value was determined based on the bimodal distribution of the mean distances for all clonotypes (mean distance = 109.0, Extended Data Fig. 5b). This threshold value was used to define 'short' and 'long' branches. For example, CT_25, categorized as a short-branch clonotype, had a mean top 10 distance of 7.8 < 109.0, whereas CT_50, categorized as a long-branch clonotype, had a corresponding value of 196.4 > 109.0.

Entropy analysis

Shannon entropy of V and J gene usage was calculated using the "Entropy" function of R package DescTools (version 0.99.58). Entropy values were normalized by calculating the maximum possible entropy for given numbers of V and J genes and independent clonotypes using a custom script. The numbers of possible V and J genes were retrieved from CellRanger 3.1.0 VDJ database.

Retrovirus production and transduction

To generate non-fluorescent TCRab-expressing vectors, the IRES-EGFP site was cut out from retroviral vector pMSCV-IRES-GFP II (pMIG II, Addgene, #52107) with restriction enzymes and replaced with synthesized DNA encoding TCRβ-P2A-TCRα. The vector was transfected into Plat-E packaging cells using the calcium phosphate precipitation method. A transfection mixture was prepared by combining 35 μg of plasmid DNA, 125 μl of 2.5 M $CaCl_2$, and 1090 μl of 0.1× TE buffer. After incubation at room temperature for 15 minutes, 1250 μl of 2× HBS buffer (100 mM HEPES, 281 mM NaCl, 1.5 mM Na_2HPO_4) was added dropwise to the DNA/$CaCl_2$ solution while vortexing. The resulting DNA/calcium phosphate precipitate was immediately added to Plat-E cells. Retrovirus in the cultured supernatant was collected 48 hours post-transfection and frozen at -80°C until use. Thawed retrovirus was transduced with Retronectin (Takara Bio) using Retronectin-bound virus infection methods according to the manufacturer's protocol. Retrovirus was transduced into mCD8αβ$^+$ BW5147.3 cells to generate TCRαβ-expressing cell lines or into mouse bone marrow (BM) cells to generate Rg mice. To establish TCRαβ-expressing BW cell lines, the transduced cells were sorted by FACS Aria II (BD Biosciences) to match the TCR expression based on the cell surface expression of CD3ε. Before all assays were performed, CD3ε or TCRβ surface level was confirmed to be matched in a group.

805 **Generation of Rg mice**
806
807 Rg mice were generated as previously described [5,78]. Briefly, BM cells were harvested from
808 CD45.1/1-*Rag2*$^{-/-}$, CD45.1/2-*Rag2*$^{-/-}$, or Thy1.1-*Rag2*$^{-/-}$ mice as indicated in figure legends, and
809 hematopoietic stem cells (HSC) were enriched by EasySep Mouse Hematopoietic Progenitor Cell
810 Isolation Kit (STEMCELL Technologies) followed by expansion in Stem cell medium
811 (StemPro™-34 SFM (Gibco), 5% FBS, 100 IU Penicillin and 100 μg/mL Streptomycin (Corning),
812 2 mM L-glutamine, with 50 ng/mL mIL-3 (STEMCELL Technologies), 50 ng/mL hIL-6
813 (STEMCELL Technologies) and 50 ng/mL mSCF (STEMCELL Technologies)) for 3 days.
814 Subsequently, HSC were transduced with retrovirus encoding TCRαβ, cultured in Stem cell
815 medium for 3 days, and then transferred into sublethally irradiated (600 rad) *Rag2*$^{-/-}$ mice using a
816 Gamma Cell 40 Cs^{137} Irradiator (Thratonics) one day before. Rg mouse blood was analyzed for
817 CD8 development and TCRβ expression by flow cytometry 6 weeks after transplantation, and
818 mice expressing more than 10% of CD8 T cells in $CD8^+$ cells were used for the generation of RgC
819 mice.
820
821
822 **Generation of RgC mice**
823
824 RgC mice were generated by adoptive transfer of naïve $CD8\beta^+CD44^-$ Rg T cells, isolated from
825 peripheral lymph nodes and spleen of Rg donor mice, into B6 (CD45.2/2, Thy1.2) recipient mice.
826 The number of transferred cells ranged from 0.5 to 10×10^4 per mouse, as indicated in figure
827 captions. To avoid potential immunogenicity associated with fluorescent proteins such as EGFP [79]
828 , we used congenic surface markers, such as CD45.1/1, CD45.1/2, and Thy1.1, as identifiers for
829 donor cells, allowing for reliable tracking of individual clones. Mixed RgC mice were generated
830 by co-transferring equal numbers of Rg T cells expressing different TCRs to minimize variability
831 across individual mice. The equal input ratios of each clone were verified by flow cytometry using
832 congenic marker expression. Single RgC mice received Rg T cells expressing a single TCR to
833 eliminate interclonal competition amongst different Rg T cell clonotypes. All RgC mice were
834 intranasally infected with PR8 one day after adoptive transfer. At >30 days post-infection,
835 transferred Rg T cells were analyzed as memory T cells by flow cytometry and RNA-Seq to assess
836 phenotype and gene expression profiles.
837
838
839 **TCR Ectodomain Constructs for X-ray Crystallography**
840
841 The design and expression of TCRαβ heterodimers has been described previously [5,23,80,81]. Briefly,
842 DNA vectors containing TCRα or TCRβ (i.e. V(D)J-C) ectodomains, a HRV3C protease cleavage
843 site [82], a base or acid leucine zipper (LZ) motif to facilitate heterodimer formation upon expression
844 [83], and a stop codon, were designed utilizing human cytomegalovirus promoter. TCRα and β
845 vectors were constructed as separate eukaryotic expression vectors using the pGDom vector from
846 prior work with TCRβ expression in mammalian cells [84,85], retaining the vector signal sequence
847 and encoding the murine Cα-HRV3C-basic-LZ or Cβ-HRV3C-acid-LZ, named as pGDomCα-LZ
848 or pGDomCβ-LZ, respectively. A novel cloning region was inserted between the signal sequence
849 and the start of the C domain utilizing two BsaI type IIS restriction endonuclease sites. This
850 allowed in-frame insertion, using Golden Gate Cloning strategies [86], of fragments encoding only

VJ-α or VDJ-β. These were isolated by PCR amplification from plasmids of full-length constructs used in retroviral transductions or purchased as double stranded DNA fragments (Azenta) and subsequently ligated into the respective pGDomCα-LZ or pGDomCβ-LZ vector. TCR clonotypes with insufficient protein yields were alternately cloned into similar vectors encoding human C-domains along with the addition of a non-native disulfide between the Cα and Cβ, resulting in a chimeric construct [87-89]. Annotated DNA and translated amino acid sequences of all constructs are included in a Supplementary Data 5.

TCR Protein Expression and Purification

The plasmids containing TCRα and TCRβ constructs were transfected together into a culture containing $2x10^6$ cells/mL Expi293F glucoseaminotransferase deficient ($GnTi^-$) cells (ThermoFisher) in fresh Expi293 Expression Medium (ThermoFisher) at a final concentration of 0.5 µg vector/mL culture each, using ExpiFectamine transfection reagent (ThermoFisher) and following the manufacturer's protocol. The Expi293F $GnTi^-$ variant produces only high mannose-modified N-linked glycans, allowing the removal of glycans under native conditions using endoglycosidase H (EndoH) [85,90]. Transfected cells were cultured at 37°C with rotary shaking at 125 rpm, per manufacturer recommendation, for 7 days for expression of protein. The supernatant was then collected and clarified by centrifugation and filtration before being passed at least twice over protein G resin (GammaBind Pl; Cytiva) coupled with the anti-LZ mAb 2H11, utilizing a gravity flow apparatus at a flow rate of approximately 1 mL/min or slower [81]. Following washing with 10 column volumes of TBS pH 8.0, bound protein was eluted with 50 mM Citrate, 500 mM NaCl buffer, pH 2.9 (adjusted with Tris base), in six 9 mL fractions, and neutralized immediately upon collection with 1 mL (i.e., 1/10 vol) 1M Tris-HCl, pH 8.0. The fractions containing eluted protein were concentrated and buffer exchanged into TBS and purified via size exclusion chromatography (SEC) utilizing a HiLoad 16/600 Superdex 200 pg column (S200P; Cytiva). Fractions containing the TCRαβ heterodimer were concentrated to 1 mg/mL, calculated via absorbance at 280 nm (A_{280}), prior to digestion with HRV3C protease (1 µg enzyme/50 µg TCR) at 25°C for 2 hours for complete removal of the LZ. Glycans were then digested with EndoH at 1U enzyme/1 µg TCR with incubation at 25°C for up to 24 hours. Completeness of the digestions was confirmed with SDS-PAGE. The fully digested protein was then purified with anion-exchange chromatography utilizing a MonoQ 5/50 column (MonoQ; Cytiva) and eluted as a single peak. Final protein purity was assessed by non-reducing (NR) and reducing SDS-PAGE prior to crystallization trials. For crystallization screening, the purified protein was buffer exchanged into 10mM Tris-HCl, pH 8.0, 100 mM NaCl and concentrated to 10 mg/mL, per A_{280} measurements.

For SM use, all constructs were the murine C domain variants with the single C-terminal interchain disulfide only. Expression and purification mirrored that for structural work with the following exceptions. Expression utilized the wildtype Expi293F cells (ThermoFisher), retaining complex glycan modifications. Following elution from 2H11 affinity columns, the proteins were buffer exchanged into PBS pH 7.4 using SEC chromatography with a 21 mL analytical-scale S200 column (Cytiva). The sample was then concentrated to approximately 1 mg/mL concentration and flash frozen with LZ regions intact for SM analysis.

897
898 **pMHC expression, refolding and complex formation, and purification**
899
900 $NP_{366-374}$ (NP366) peptide (ASNENMETM) was chemically synthesized (United Biosystems, Inc)
901 and NP366/H-2D^b production was executed similarly to that previously described [48,91,92]. Plasmids
902 containing H-2D^b or murine β2m were transformed into BL21-DE3 *E.Coli* for expression.
903 Transformed cells were grown to an OD_{600} of 0.6-0.8 in Luria broth (LB) at 37°C under agitation
904 at which point expression was induced with the addition of 0.5mM IPTG. After 3 hours, cells were
905 harvested by centrifugation, supernatant was discarded and the cell pellet was resuspended in 30
906 mL of TBS, pH 8.0, 1 mg/mL lysozyme was added, and the resuspension was frozen at -80°C for
907 at least 2 hr. The lysate was then thawed and 0.3 mg/mL of DNAse and EDTA free protease
908 inhibitor (Roche) were added before being frozen again at -80°C > 2 hr or overnight. The lysate
909 was thawed, and inclusion bodies were purified via centrifugation and resuspension cycles,
910 washing twice with TBS, twice with TBS + 0.1% TritonX-100, and once with TBS. The final
911 product was a pure inclusion body pellet, which was dissolved in 10 mL of 5.4M Guanidine HCl,
912 0.1M Tris, pH 8.0. The solution was centrifuged and the supernatant was collected before the
913 addition of dithiothreitol to 2 mM and storage at -80°C. H-2D^b, β2M, and NP366 peptide were
914 added to 300 mL 20 mM Tris, 8M Urea at a 60:20:10 w/w ratio before serial dialysis (6-8 KDa
915 nominal molecular weight cutoff; Spectrum Laboratories, Inc.) against 4 L of 20 mM Tris + 2 M,
916 1M, 0.5M and 0M Urea, with each step greater than 2 h or overnight for a total of at least 48 hours
917 dialysis/refold time. The dialyzed refolded protein was then concentrated for purification via SEC
918 (S200P; Cytiva) followed by anion-exchange chromatography (MonoQ; Cytiva). The final
919 purification yielded a mono-dispersed peak and subsequent NR SDS-PAGE revealed two bands,
920 corresponding to H-2D^b and β2M. For crystallization screening, the purified protein was buffer
921 exchanged into 10 mM Tris-HCl, pH 8.0, 100 mM NaCl and concentrated to 10 mg/mL, per A_{280}
922 measurements.
923
924
925 **SM assay**
926
927 Tether geometry and optical tweezers measurements were carried out essentially as detailed in [23],
928 and as shown schematically in Figure (Extended Data Fig. 6a). Streptavidin-coated polystyrene
929 beads (1.29 µm diameter, Spherotech Inc) were connected to biotin terminated 1010-bp double-
930 stranded DNA containing covalently bound 2H11 antibody that binds to the TCRαβ construct
931 paired LZ region. Incubation time and DNA concentration were varied to control tether density
932 around the bead, which was optimized for the binding probability of each individual TCRαβ-
933 pMHC pair. After incubation at RT with DNA tethers, DNA-labeled beads were washed then
934 resuspended in 15 µL of TCRαβ (~0.1 mg/mL) and incubated at RT for an additional 1 hr. The
935 tethered beads were then washed a final time before resuspension in PBS buffer.
936 A 10-µL flow cell was prepared using two pieces of double-sided sticky tape. Cover-glass
937 surfaces were coated with functionalized PEG silane 99% mixed with 1% biotin-PEG silane like
938 previously described work [23]. Casein blocker (0.1 mg/mL) was introduced to the flow cell for 10
939 minutes then washed out with PBS buffer. Streptavidin (0.5 mg/mL) was introduced into the flow
940 cell, incubated for 30 min, and washed with PBS buffer. Biotinylated pMHC (~0.05 mg/mL) was
941 introduced and incubated for 30 min and washed again with PBS buffer. Finally, tethered bead
942 solution was introduced to the flow cell for bond lifetime measurements.

943 Tethers were formed by scanning a bead near the cover-glass surface using 300 nm steps
944 of the piezo stage in the x-y plane, pausing for several seconds between stage movements to allow
945 for TCRαβ-pMHC bond formation (Extended Data Fig. 6b). Successful tether formation was
946 indicated by bead displacement relative to the trap center. After rupture, beads were mapped for
947 position sensing using automated procedures followed by stiffness calibration. Control
948 experiments were TCRαβ was omitted from the assay resulted in minimal, atypical tether
949 formation. Binding probability can be assessed by comparing the number of stage movements
950 which resulted in a binding event to the total number of stage movements.
951
952
953 **Peptide stimulation and IL-2 measurement**
954
955 $1x10^5$ NP-specific TCR-transduced BW cells were cultured in D10 with 1μg/mL WT-$NP_{366-374}$,
956 1mg/mL $NP_{366-374}$ peptide variants, or titrated theses peptides (from $1x10^{-5}$ to $1x10^4$ ng/mL) at
957 37°C for 16-18 hours overnight. $1x10^5$ R8 cells used as APC were treated with Mitomycin C
958 (Sigma-Aldrich) and washed with PBS three times prior to use. IL-2 concentration in culture
959 supernatant was measured by ELISA assay according to the manufacturer's instruction. EC_{50} of
960 peptide response to each BW cells was calculated by Prism 10 (GraphPad Software).
961
962
963 **Tetramer activation assay and pTyr analysis**
964
965 Detection of CD3 subunits, pTyr, and CD3ζ pTyr142 pre- and post-tetramer activation was carried
966 out using 5 x 10^6 cells/ml in DMEM. WT $NP_{366-374}/D^b$ tetramer (0.75 μg/ml final concentration)
967 was added to the NP202 or NP105 cell samples matched for cell-surface TCR level expression
968 prior to use. Control samples were simultaneously prepared for each cell line without the addition
969 of tetramer at time zero. All cell samples were incubated on ice for 20 min and then washed with
970 DMEM to remove unbound tetramer. The cells were resuspended at a final concentration of 2 x
971 10^6 cells per 0.1 mL and incubated at 37◦C for 1 min. Then, 1 mL of ice-cold PBS was added to
972 the cells and the cells were pelleted at 1200 rpm for 5 min. The PBS wash was removed and lysis
973 buffer (1% Triton X-100, 0.1% SDS, 50 mM Tris (pH 7.4), 150 mM NaCl, 2 mM NaVO3, 1 mM
974 N-ethylmaleimide, and Roche cØmplete protease cocktail) was added to the cell pellet. The
975 resuspended samples were immediately placed on dry ice to await further processing.
976 For analysis of CD3 and phosphorylated proteins, cell samples were then thawed for 10
977 min on ice and centrifuged at 13,000 rpm, 4◦C for 15 min. The clarified lysate was transferred to
978 a clean tube. Aliquots were separated non-reducing with 4-12% bis-tris NuPAGE gels, transferred
979 to polyvinylidene difluoride (PVDF) membrane, and detected with anti-CD3ζ pTyr142 (clone EM-
980 54), and anti-CD3ζ (clone H146-968). The western blots were imaged using a Bio-Rad ChemiDoc
981 imaging system. Band density was measured using the Image Lab software, with band densities
982 normalized to the median within each experimental set to mitigate antibody staining artifacts The
983 level of phosphorylated CD3ζ Tyr142 was determined in proportion to CD3ζ for each sample.
984 Three biological replicates were prepared for each activation assay with tetramer activation being
985 carried out on three separate days with three separate cell culture preparations. To examine overall
986 phosphotyrosine levels, the cell lysates were separated on a reducing gel, transferred to PVDF
987 membrane, and assayed for pTyr (clone 4G10).
988

Bulk RNA-seq analyses

Following phenotyping and gating for lymph node cells of retrogenic origin (see table below), cells were sorted into 1.5 mL tubes containing TCL buffer x2 (350 µL; Qiagen) supplemented with 2-mercaptoethanol (1%).

Gating parameters and cell yields for retrogenic cells:

C101	Gating: viable CD8β$^+$CD45.1$^+$/CD45.2$^+$;						host: B6 (CD45.2$^+$)
Mouse:	1	2	3	4	5	6	7
Cell yield:	5,517	2,852	7,515	8,758	16,051	992	2,658

C105	Gating: viable CD8β$^+$CD45.1$^+$;						host: B6 (CD45.2$^+$)
Mouse:	1A	2	4	5	6	7	1B (CD45.1^{int})
Cell yield:	1,222	275	227	504	5,517	7,165	7,305

C202	Gating: viable CD8β$^+$Thy1.1$^+$;					host: B6 (Thy1.2$^+$)
Mouse:	1	2	3	5	6	7
Cell yield:	6,695	1,183	2,172	3,108	7,011	5,065

C204	Gating: viable CD8β$^+$CD45.1$^+$;			host: B6 (CD45.2$^+$)
Mouse:	2	3	5	6
Cell yield:	3.088	347	5,203	5,418

C207	Gating: viable CD8β$^+$CD45.1$^+$/CD45.2$^+$;			host: B6 (CD45.2$^+$)
Mouse:	2	3	4	5
Cell yield:	2,306	11,467	10,620	7,549

Total RNA was extracted from each sample (n = 28) using the Arcturus Pico Pure RNA kit (ThermoFisher) following the manufacturer's protocol including on-column RNase-free DNase treatment (27 Kunitz units/sample; Qiagen), and eluting into 11 µL elution buffer, snap freezing at -80ºC and storage at the same temperature until library preparation and sequencing (Admera Health, LLC). Following initial RNA preparation quality control, libraries were prepared using the SMART-Seq v4 Ultra Low Input kit with Tagmentation (Takara Bio USA, Inc.), Illumina adapters added, and sequenced on the NovaSeq X Plus platform (2 x 250 bp paired end sequencing, 40 x 10^6 reads/sample). The paired output fasta files for each sample were checked for quality using FastQC, and adapters trimmed using FastqMcf and Cutadapt [93]. Contaminating non-polyA-tailed RNA sequence, mitochondrial genome sequences, ribosomal RNAs and transfer RNAs were then removed using Bowtie2 [94] and the resulting filtered reads aligned to the mouse reference genome assembly GRCm39 using STAR (v2.7.3a) [95]. HTSeq-count was then used to count the reads aligned to each gene. Gene expression in transcripts per million (tpm) normalizing for transcript length and library size, was obtained using the DESeq2 package under Bioconductor version 3.21 running on the R version 4.5 platform. All further processing for hierarchical clustering and heat maps, and differential gene expression (DESeq2), was performed on the same platform. Note that for Extended Data Fig. 10e, the heat maps represent transcripts per million (tpm) for a reduced panel of transcripts representing genes validated as upregulated on T cell activation. In this

instance, tpm can be used as a broad measure for comparison of the two data sets (C101/C105 and C202/C204/C207) since all samples were of similar origin (mLN $CD8^+$ retrogenic T cells), and identical RNA preparation, sequencing, and quality control statistics (e.g. mitochondrial transcript representation) [96]. All data was organized/plotted using MS-Excel or plotted using PSI-Plot version 9 (Poly Software International).

Crystallization

Each NP TCR was mixed with NP366-H-2D^b ($NP_{366-374}/D^b$) in a 1:1 molar ratio. The mixed TCR-pMHC solution was concentrated to about 10-20mg/ml. Sitting drop vapor diffusion technique in 96-well CrystalQuick plates (Greiner) was used for crystallization trials with the help of a Mosquito nanoliter liquid handler (TTP LabTech) at 16°C. For each condition, 0.4 mL of crystallization screening formulation was added to 0.4 ml of concentrated TCR-pMHC solution; the mixture was equilibrated against 140 mL of the same screening buffer in each reservoir well. The crystallization screens used were MCSG-1-4 (Anatrace), Peg/Ion (Hampton Research) and Top96 (Molecular Dimensions). Crystals appeared under the conditions 1-8 as listed for each construct:

1) NP101-NP366/H-2D^b (mouse/human hybrid TCR) = NP101-$NP_{336-374}/D^b$
   0.2 M Ammonium iodide pH 6.2, 20% (w/v) PEG 3,350.

2) NP105-NP366/H-2D^b (mouse/human hybrid TCR) = NP105-$NP_{336-374}/D^b$
   0.1 M Sodium citrate, 5% (v/v) 2-Propanol, 20% (w/v) PEG 4,000,

3) NP202 apo form (mouse TCR)
   0.2 M Ammonium nitrate pH 6.2, 20% (w/v) PEG 3,350.

4) NP202-NP366/H-2D^b (mouse TCR) = NP202-$NP_{336-374}/D^b$
   0.1 M Tris hydrochloride pH 8.5, 8% (w/v) PEG 8,000.

5) NP203-NP366/H-2D^b (mouse/human hybrid TCR) = NP203-$NP_{336-374}/D^b$
   0.2 M Ammonium fluoride pH 6.2, 20% (w/v) PEG 3,350.

6) NP204-NP366/H-2D^b (mouse TCR) = NP204-$NP_{336-374}/D^b$
   1% (w/v) Tryptone, 0.05 M HEPES sodium pH 7.0, 12% (w/v) PEG 3,350.

7) NP207 apo form (mouse TCR)
   0.2 M Potassium Nitrate: HCl pH 6.9, 20% (w/v) PEG 3,350.

8) NP207-NP366/H-2D^b (mouse/human hybrid TCR) = NP207-$NP_{336-374}/D^b$
   0.6 M Sodium Chloride, 0.1 M MES:NaOH pH 6.5, 20% (w/v) PEG 4,000.

1081 **X-ray diffraction data collection and processing**
1082
1083 All crystals were harvested and treated with a cryoprotectant solution (25% glycerol or 25%
1084 ethylene glycol in mother liquor) and then flash-frozen in liquid nitrogen before X-ray diffraction
1085 data collection. Those data were collected at 100 K from the cryocooled crystals at the 19-ID at
1086 the 19-ID (SBC) beamline of the Advanced Photon Source at Argonne National Laboratory or 19-
1087 ID (NYX) beamline or 17-ID-2 (FMX) beamline of National Synchrotron Light Source II at the
1088 Brookhaven National Laboratory. The intensities of each data set were integrated, scaled, and
1089 merged with the HKL-3000 program suite [97]. The structure of NP202-NP366-H-2D^b (NP202-
1090 NP$_{366-374}$/D^b) was first determined using the molecular replacement (MR) method [98], in which the
1091 murine P14 TCR and the H-2D^b from their complex (PDB code: 5M01) were used as search
1092 templates (Supplementary Table 2). The following structural determination of NP TCR apo forms
1093 and other complexes were performed with the same MR method using NP202 TCR and H-2D^b
1094 obtained in NP202-NP366-H-2D^b complex (NP202-NP$_{366-374}$/D^b) that was determined and refined
1095 in the first place. All the models from structural determination were rebuilt using the program
1096 Coot [99]. The final models was refined using the program phenix.refine [100]. Structural validation
1097 of each model was performed using the program MolProbity [101].
1098
1099
1100 **Molecular dynamics simulation**
1101
1102 Molecular dynamics simulation under force was performed based on the method described in [40].
1103 Structure preparation, preparatory simulation, and trajectory analysis were performed by using
1104 CHARMM [102] and production runs were performed by using OpenMM [103]. Briefly, crystal
1105 structures of NP202, NP101, NP207, and NP203 complexed with NP$_{366-374}$ /H-2D^b were prepared
1106 by converting the Cα, and Cβ sequences from human (used for x-ray crystallography) to mouse
1107 (used for other experiments). The structure of NP202 had the full mouse sequence except for S184
1108 of Cβ, which was mutated to C184 for mouse. The resulting structure of the C-module was aligned
1109 and copied to NP101, NP207, and NP203 to generate the mouse versions. 5-residue long linkers
1110 were added to the C-terminal ends of MHC and the TCR based on their amino acid sequences so
1111 that the last residues were Y283 for MHC, T214 for Cα, and A245 for Cβ, respectively. C_α atoms
1112 of the terminal residues were harmonically restrained at 168-Å extensions to apply fluctuating
1113 loads that are comparable in magnitude to those used in single-molecule experiments. We modified
1114 the contact analysis method developed in [26] to examine intradomain contacts as shown in
1115 Supplementary Discussion Item 5. Additional simulations and more extensive analyses will be
1116 published elsewhere.
1117
1118
1119 **Statistics**
1120
1121 Statistical tests used throughout this study are indicated in figure captions or the main text. Paired
1122 t-tests were used for RgC mouse and p-tyrosine experiments. Chi-squared tests were employed for
1123 analysis of T_{CM} vs. T_{EM} clonotype distributions, Shannon entropy, and RNA-seq clustering. Mann–
1124 Whitney U-tests evaluated differences in cell counts. Trend tests assessed graded gene expression
1125 across cell–clonotype categories. Two-sided Fisher's exact tests were used for cross-reactive

clonotype comparisons. Gene Set Enrichment Analysis (GSEA) was evaluated by a permutation test.

Data and materials availability

Sequence files for scRNA-Seq of $NP_{366-374}/D^b$-specific memory CD8 T cells, non-tetramer sorted CD8 T cells at memory phase, and at recall response have been deposited in NCBI Gene Expression Omnibus (GEO) under accession GSE302680. Bulk RNAseq data are accession GSE302856. PDB accession code will be available at the time of publication for all X-ray crystallographic structures. Materials and protocols are available on request to scientists through the corresponding authors.

References

1 Kaech, S. M. & Cui, W. Transcriptional control of effector and memory CD8+ T cell differentiation. *Nat Rev Immunol* **12**, 749-761 (2012). https://doi.org/10.1038/nri3307

2 Wherry, E. J. & Ahmed, R. Memory CD8 T-cell differentiation during viral infection. *J Virol* **78**, 5535-5545 (2004). https://doi.org/10.1128/JVI.78.11.5535-5545.2004

3 Sallusto, F., Geginat, J. & Lanzavecchia, A. Central memory and effector memory T cell subsets: function, generation, and maintenance. *Annu Rev Immunol* **22**, 745-763 (2004). https://doi.org/10.1146/annurev.immunol.22.012703.104702

4 Jameson, S. C. & Masopust, D. Understanding Subset Diversity in T Cell Memory. *Immunity* **48**, 214-226 (2018). https://doi.org/10.1016/j.immuni.2018.02.010

5 Akitsu, A. *et al.* Parsing digital or analog TCR performance through piconewton forces. *Sci Adv* **10**, eado4313 (2024). https://doi.org/10.1126/sciadv.ado4313

6 La Gruta, N. L. *et al.* A virus-specific CD8+ T cell immunodominance hierarchy determined by antigen dose and precursor frequencies. *Proc Natl Acad Sci U S A* **103**, 994-999 (2006). https://doi.org/10.1073/pnas.0510429103

7 Zhou, X. *et al.* Differentiation and persistence of memory CD8(+) T cells depend on T cell factor 1. *Immunity* **33**, 229-240 (2010). https://doi.org/10.1016/j.immuni.2010.08.002

8 Zhou, X. & Xue, H. H. Cutting edge: generation of memory precursors and functional memory CD8+ T cells depends on T cell factor-1 and lymphoid enhancer-binding factor-1. *J Immunol* **189**, 2722-2726 (2012). https://doi.org/10.4049/jimmunol.1201150

9 Yang, C. Y. *et al.* The transcriptional regulators Id2 and Id3 control the formation of distinct memory CD8+ T cell subsets. *Nat Immunol* **12**, 1221-1229 (2011). https://doi.org/10.1038/ni.2158

10 Wherry, E. J. *et al.* Lineage relationship and protective immunity of memory CD8 T cell subsets. *Nat Immunol* **4**, 225-234 (2003). https://doi.org/10.1038/ni889

1167 11 Jeannet, G. *et al.* Essential role of the Wnt pathway effector Tcf-1 for the
1168 establishment of functional CD8 T cell memory. *Proc Natl Acad Sci U S A* **107**, 9777-
1169 9782 (2010). https://doi.org/10.1073/pnas.0914127107
1170 12 Cannarile, M. A. *et al.* Transcriptional regulator Id2 mediates CD8+ T cell immunity.
1171 *Nat Immunol* **7**, 1317-1325 (2006). https://doi.org/10.1038/ni1403
1172 13 Omilusik, K. D. *et al.* Sustained Id2 regulation of E proteins is required for terminal
1173 differentiation of effector CD8(+) T cells. *J Exp Med* **215**, 773-783 (2018).
1174 https://doi.org/10.1084/jem.20171584
1175 14 Hamilton, S. E. & Jameson, S. C. CD8 T cell memory: it takes all kinds. *Front*
1176 *Immunol* **3**, 353 (2012). https://doi.org/10.3389/fimmu.2012.00353
1177 15 van der Windt, G. J. & Pearce, E. L. Metabolic switching and fuel choice during T-cell
1178 differentiation and memory development. *Immunol Rev* **249**, 27-42 (2012).
1179 https://doi.org/10.1111/j.1600-065X.2012.01150.x
1180 16 Marzo, A. L. *et al.* Initial T cell frequency dictates memory CD8+ T cell lineage
1181 commitment. *Nat Immunol* **6**, 793-799 (2005). https://doi.org/10.1038/ni1227
1182 17 Obar, J. J. & Lefrancois, L. Early signals during CD8 T cell priming regulate the
1183 generation of central memory cells. *J Immunol* **185**, 263-272 (2010).
1184 https://doi.org/10.4049/jimmunol.1000492
1185 18 Badovinac, V. P., Haring, J. S. & Harty, J. T. Initial T cell receptor transgenic cell
1186 precursor frequency dictates critical aspects of the CD8(+) T cell response to
1187 infection. *Immunity* **26**, 827-841 (2007).
1188 https://doi.org/10.1016/j.immuni.2007.04.013
1189 19 Daniels, M. A. & Teixeiro, E. TCR Signaling in T Cell Memory. *Front Immunol* **6**, 617
1190 (2015). https://doi.org/10.3389/fimmu.2015.00617
1191 20 Smith-Garvin, J. E. *et al.* T-cell receptor signals direct the composition and function
1192 of the memory CD8+ T-cell pool. *Blood* **116**, 5548-5559 (2010).
1193 https://doi.org/10.1182/blood-2010-06-292748
1194 21 Solouki, S. *et al.* TCR Signal Strength and Antigen Affinity Regulate CD8(+) Memory T
1195 Cells. *J Immunol* **205**, 1217-1227 (2020). https://doi.org/10.4049/jimmunol.1901167
1196 22 Brazin, K. N. *et al.* The T Cell Antigen Receptor alpha Transmembrane Domain
1197 Coordinates Triggering through Regulation of Bilayer Immersion and CD3 Subunit
1198 Associations. *Immunity* **49**, 829-841 e826 (2018).
1199 https://doi.org/10.1016/j.immuni.2018.09.007
1200 23 Das, D. K. *et al.* Force-dependent transition in the T-cell receptor beta-subunit
1201 allosterically regulates peptide discrimination and pMHC bond lifetime. *Proc Natl*
1202 *Acad Sci U S A* **112**, 1517-1522 (2015). https://doi.org/10.1073/pnas.1424829112
1203 24 Feng, Y. *et al.* Mechanosensing drives acuity of alphabeta T-cell recognition. *Proc*
1204 *Natl Acad Sci U S A* **114**, E8204-E8213 (2017).
1205 https://doi.org/10.1073/pnas.1703559114
1206 25 Feng, Y., Reinherz, E. L. & Lang, M. J. alphabeta T Cell Receptor Mechanosensing
1207 Forces out Serial Engagement. *Trends Immunol* **39**, 596-609 (2018).
1208 https://doi.org/10.1016/j.it.2018.05.005
1209 26 Hwang, W., Mallis, R. J., Lang, M. J. & Reinherz, E. L. The alphabetaTCR
1210 mechanosensor exploits dynamic ectodomain allostery to optimize its ligand

1211 recognition site. *Proc Natl Acad Sci U S A* **117**, 21336-21345 (2020).
1212 https://doi.org/10.1073/pnas.2005899117
1213 27 Kim, S. T. *et al.* The alphabeta T cell receptor is an anisotropic mechanosensor. *J Biol*
1214 *Chem* **284**, 31028-31037 (2009). https://doi.org/10.1074/jbc.M109.052712
1215 28 Liu, B., Chen, W., Evavold, B. D. & Zhu, C. Accumulation of dynamic catch bonds
1216 between TCR and agonist peptide-MHC triggers T cell signaling. *Cell* **157**, 357-368
1217 (2014). https://doi.org/10.1016/j.cell.2014.02.053
1218 29 Wu, P. *et al.* Mechano-regulation of Peptide-MHC Class I Conformations
1219 Determines TCR Antigen Recognition. *Mol Cell* **73**, 1015-1027 e1017 (2019).
1220 https://doi.org/10.1016/j.molcel.2018.12.018
1221 30 Zhao, X. *et al.* Tuning T cell receptor sensitivity through catch bond engineering.
1222 *Science* **376**, eabl5282 (2022). https://doi.org/10.1126/science.abl5282
1223 31 Mallis, R. J. *et al.* Biophysical and Structural Features of alphabetaT-Cell Receptor
1224 Mechanosensing: A Paradigmatic Shift in Understanding T-Cell Activation. *Immunol*
1225 *Rev* **329**, e13432 (2025). https://doi.org/10.1111/imr.13432
1226 32 Hu, Y., Duan, Y. & Salaita, K. DNA Nanotechnology for Investigating Mechanical
1227 Signaling in the Immune System. *Angew Chem Int Ed Engl* **62**, e202302967 (2023).
1228 https://doi.org/10.1002/anie.202302967
1229 33 Dash, P. *et al.* Quantifiable predictive features define epitope-specific T cell
1230 receptor repertoires. *Nature* **547**, 89-93 (2017). https://doi.org/10.1038/nature22383
1231 34 Sridhar, S. *et al.* Cellular immune correlates of protection against symptomatic
1232 pandemic influenza. *Nat Med* **19**, 1305-1312 (2013).
1233 https://doi.org/10.1038/nm.3350
1234 35 Valkenburg, S. A. *et al.* Molecular basis for universal HLA-A*0201-restricted CD8+ T-
1235 cell immunity against influenza viruses. *Proc Natl Acad Sci U S A* **113**, 4440-4445
1236 (2016). https://doi.org/10.1073/pnas.1603106113
1237 36 Zhong, W. *et al.* Significant impact of sequence variations in the nucleoprotein on
1238 CD8 T cell-mediated cross-protection against influenza A virus infections. *PLoS One*
1239 **5**, e10583 (2010). https://doi.org/10.1371/journal.pone.0010583
1240 37 Young, A. C., Zhang, W., Sacchettini, J. C. & Nathenson, S. G. The three-dimensional
1241 structure of H-2Db at 2.4 A resolution: implications for antigen-determinant
1242 selection. *Cell* **76**, 39-50 (1994). https://doi.org/10.1016/0092-8674(94)90171-6
1243 38 Garcia, K. C. *et al.* An alphabeta T cell receptor structure at 2.5 A and its orientation
1244 in the TCR-MHC complex. *Science* **274**, 209-219 (1996).
1245 https://doi.org/10.1126/science.274.5285.209
1246 39 Chang-Gonzalez, A. C. *et al.* Load-based divergence in the dynamic allostery of two
1247 TCRs recognizing the same pMHC. *Elife* **13** (2025).
1248 https://doi.org/10.7554/eLife.104280
1249 40 Chang-Gonzalez, A. C., Mallis, R. J., Lang, M. J., Reinherz, E. L. & Hwang, W.
1250 Asymmetric framework motion of TCRalphabeta controls load-dependent peptide
1251 discrimination. *Elife* **13** (2024). https://doi.org/10.7554/eLife.91881
1252 41 Chan, A. C., Irving, B. A., Fraser, J. D. & Weiss, A. The zeta chain is associated with a
1253 tyrosine kinase and upon T-cell antigen receptor stimulation associates with ZAP-

70, a 70-kDa tyrosine phosphoprotein. *Proc Natl Acad Sci U S A* **88**, 9166-9170 (1991). https://doi.org/10.1073/pnas.88.20.9166

42 Sen, D. R. *et al.* The epigenetic landscape of T cell exhaustion. *Science* **354**, 1165-1169 (2016). https://doi.org/10.1126/science.aae0491

43 Kurtulus, S. *et al.* Checkpoint Blockade Immunotherapy Induces Dynamic Changes in PD-1(-)CD8(+) Tumor-Infiltrating T Cells. *Immunity* **50**, 181-194 e186 (2019). https://doi.org/10.1016/j.immuni.2018.11.014

44 Abdullah, L. *et al.* The endogenous antigen-specific CD8(+) T cell repertoire is composed of unbiased and biased clonotypes with differential fate commitments. *Immunity* **58**, 601-615 e609 (2025). https://doi.org/10.1016/j.immuni.2025.02.001

45 Notti, R. Q. *et al.* The resting and ligand-bound states of the membrane-embedded human T-cell receptor-CD3 complex. *bioRxiv* (2024). https://doi.org/10.1101/2023.08.22.554360

46 von Boehmer, H. Unique features of the pre-T-cell receptor alpha-chain: not just a surrogate. *Nat Rev Immunol* **5**, 571-577 (2005). https://doi.org/10.1038/nri1636

47 Das, D. K. *et al.* Pre-T Cell Receptors (Pre-TCRs) Leverage Vbeta Complementarity Determining Regions (CDRs) and Hydrophobic Patch in Mechanosensing Thymic Self-ligands. *J Biol Chem* **291**, 25292-25305 (2016). https://doi.org/10.1074/jbc.M116.752865

48 Mallis, R. J., Arthanari, H., Lang, M. J., Reinherz, E. L. & Wagner, G. NMR-directed design of pre-TCRbeta and pMHC molecules implies a distinct geometry for pre-TCR relative to alphabetaTCR recognition of pMHC. *J Biol Chem* **293**, 754-766 (2018). https://doi.org/10.1074/jbc.M117.813493

49 Li, X. *et al.* Pre-T cell receptors topologically sample self-ligands during thymocyte beta-selection. *Science* **371**, 181-185 (2021). https://doi.org/10.1126/science.abe0918

50 Borowski, C., Li, X., Aifantis, I., Gounari, F. & von Boehmer, H. Pre-TCRalpha and TCRalpha are not interchangeable partners of TCRbeta during T lymphocyte development. *J Exp Med* **199**, 607-615 (2004). https://doi.org/10.1084/jem.20031973

51 Gounari, F. & Khazaie, K. TCF-1: a maverick in T cell development and function. *Nat Immunol* **23**, 671-678 (2022). https://doi.org/10.1038/s41590-022-01194-2

52 Hong, C., Luckey, M. A. & Park, J. H. Intrathymic IL-7: the where, when, and why of IL-7 signaling during T cell development. *Semin Immunol* **24**, 151-158 (2012). https://doi.org/10.1016/j.smim.2012.02.002

53 Kaech, S. M. *et al.* Selective expression of the interleukin 7 receptor identifies effector CD8 T cells that give rise to long-lived memory cells. *Nat Immunol* **4**, 1191-1198 (2003). https://doi.org/10.1038/ni1009

54 Miyazaki, M. *et al.* The opposing roles of the transcription factor E2A and its antagonist Id3 that orchestrate and enforce the naive fate of T cells. *Nat Immunol* **12**, 992-1001 (2011). https://doi.org/10.1038/ni.2086

55 Zhang, N., Hartig, H., Dzhagalov, I., Draper, D. & He, Y. W. The role of apoptosis in the development and function of T lymphocytes. *Cell Res* **15**, 749-769 (2005). https://doi.org/10.1038/sj.cr.7290345

56 Dunkle, A., Dzhagalov, I., Gordy, C. & He, Y. W. Transfer of CD8+ T cell memory using Bcl-2 as a marker. *J Immunol* **190**, 940-947 (2013). https://doi.org/10.4049/jimmunol.1103481

57 Bohineust, A., Garcia, Z., Beuneu, H., Lemaitre, F. & Bousso, P. Termination of T cell priming relies on a phase of unresponsiveness promoting disengagement from APCs and T cell division. *J Exp Med* **215**, 1481-1492 (2018). https://doi.org/10.1084/jem.20171708

58 Mempel, T. R., Henrickson, S. E. & Von Andrian, U. H. T-cell priming by dendritic cells in lymph nodes occurs in three distinct phases. *Nature* **427**, 154-159 (2004). https://doi.org/10.1038/nature02238

59 Miller, M. J., Wei, S. H., Parker, I. & Cahalan, M. D. Two-photon imaging of lymphocyte motility and antigen response in intact lymph node. *Science* **296**, 1869-1873 (2002). https://doi.org/10.1126/science.1070051

60 Ding, Y. H., Baker, B. M., Garboczi, D. N., Biddison, W. E. & Wiley, D. C. Four A6-TCR/peptide/HLA-A2 structures that generate very different T cell signals are nearly identical. *Immunity* **11**, 45-56 (1999). https://doi.org/10.1016/s1074-7613(00)80080-1

61 Hodavance, S. Y., Gareri, C., Torok, R. D. & Rockman, H. A. G Protein-coupled Receptor Biased Agonism. *J Cardiovasc Pharmacol* **67**, 193-202 (2016). https://doi.org/10.1097/FJC.0000000000000356

62 Erdogmus, S. *et al.* Helix 8 is the essential structural motif of mechanosensitive GPCRs. *Nat Commun* **10**, 5784 (2019). https://doi.org/10.1038/s41467-019-13722-0

63 Furness, S. G. & Sexton, P. M. Coding GPCR-G protein specificity. *Cell Res* **27**, 1193-1194 (2017). https://doi.org/10.1038/cr.2017.92

64 Wu, T. *et al.* Quantification of epitope abundance reveals the effect of direct and cross-presentation on influenza CTL responses. *Nat Commun* **10**, 2846 (2019). https://doi.org/10.1038/s41467-019-10661-8

65 Householder, K. D. *et al.* De novo design and structure of a peptide-centric TCR mimic binding module. *Science* **389**, 375-379 (2025). https://doi.org/10.1126/science.adv3813

66 Johansen, K. H. *et al.* De novo-designed pMHC binders facilitate T cell-mediated cytotoxicity toward cancer cells. *Science* **389**, 380-385 (2025). https://doi.org/10.1126/science.adv0422

67 Liu, B. *et al.* Design of high-specificity binders for peptide-MHC-I complexes. *Science* **389**, 386-391 (2025). https://doi.org/10.1126/science.adv0185

68 Zheng, G. X. *et al.* Massively parallel digital transcriptional profiling of single cells. *Nat Commun* **8**, 14049 (2017). https://doi.org/10.1038/ncomms14049

69 Hao, Y. *et al.* Integrated analysis of multimodal single-cell data. *Cell* **184**, 3573-3587 e3529 (2021). https://doi.org/10.1016/j.cell.2021.04.048

70 Wolock, S. L., Lopez, R. & Klein, A. M. Scrublet: Computational Identification of Cell Doublets in Single-Cell Transcriptomic Data. *Cell Syst* **8**, 281-291 e289 (2019). https://doi.org/10.1016/j.cels.2018.11.005

71 Aibar, S. *et al.* SCENIC: single-cell regulatory network inference and clustering. *Nat Methods* **14**, 1083-1086 (2017). https://doi.org/10.1038/nmeth.4463

72 McInnes, L., Healy, J., Saul, N. & Großberger, L. UMAP: Uniform Manifold Approximation and Projection. *Journal of Open Source Software* **3 (29)**, 861 (2018). https://doi.org/10.21105/joss.00861

73 Hudson, W. H. *et al.* Expression of novel long noncoding RNAs defines virus-specific effector and memory CD8(+) T cells. *Nat Commun* **10**, 196 (2019). https://doi.org/10.1038/s41467-018-07956-7

74 Xu, S. *et al.* Using clusterProfiler to characterize multiomics data. *Nat Protoc* **19**, 3292-3320 (2024). https://doi.org/10.1038/s41596-024-01020-z

75 La Manno, G. *et al.* RNA velocity of single cells. *Nature* **560**, 494-498 (2018). https://doi.org/10.1038/s41586-018-0414-6

76 Weiler, P., Lange, M., Klein, M., Pe'er, D. & Theis, F. CellRank 2: unified fate mapping in multiview single-cell data. *Nat Methods* **21**, 1196-1205 (2024). https://doi.org/10.1038/s41592-024-02303-9

77 Mayer-Blackwell, K. *et al.* TCR meta-clonotypes for biomarker discovery with tcrdist3 enabled identification of public, HLA-restricted clusters of SARS-CoV-2 TCRs. *Elife* **10** (2021). https://doi.org/10.7554/eLife.68605

78 Holst, J. *et al.* Generation of T-cell receptor retrogenic mice. *Nat Protoc* **1**, 406-417 (2006). https://doi.org/10.1038/nprot.2006.61

79 Agudo, J. *et al.* GFP-specific CD8 T cells enable targeted cell depletion and visualization of T-cell interactions. *Nat Biotechnol* **33**, 1287-1292 (2015). https://doi.org/10.1038/nbt.3386

80 Chang, H. C. *et al.* A general method for facilitating heterodimeric pairing between two proteins: application to expression of alpha and beta T-cell receptor extracellular segments. *Proc Natl Acad Sci U S A* **91**, 11408-11412 (1994). https://doi.org/10.1073/pnas.91.24.11408

81 Liu, J. *et al.* Crystallization of a deglycosylated T cell receptor (TCR) complexed with an anti-TCR Fab fragment. *J Biol Chem* **271**, 33639-33646 (1996). https://doi.org/10.1074/jbc.271.52.33639

82 Waugh, D. S. An overview of enzymatic reagents for the removal of affinity tags. *Protein Expr Purif* **80**, 283-293 (2011). https://doi.org/10.1016/j.pep.2011.08.005

83 O'Shea, E. K., Lumb, K. J. & Kim, P. S. Peptide 'Velcro': design of a heterodimeric coiled coil. *Curr Biol* **3**, 658-667 (1993). https://doi.org/10.1016/0960-9822(93)90063-t

84 Tiller, T., Busse, C. E. & Wardemann, H. Cloning and expression of murine Ig genes from single B cells. *J Immunol Methods* **350**, 183-193 (2009). https://doi.org/10.1016/j.jim.2009.08.009

85 Mallis, R. J. *et al.* Efficient and economic protein labeling for NMR in mammalian expression systems: Application to a preT-cell and T-cell receptor protein. *Protein Sci* **33**, e4950 (2024). https://doi.org/10.1002/pro.4950

86 Engler, C., Kandzia, R. & Marillonnet, S. A one pot, one step, precision cloning method with high throughput capability. *PLoS One* **3**, e3647 (2008). https://doi.org/10.1371/journal.pone.0003647

87 Boulter, J. M. *et al.* Stable, soluble T-cell receptor molecules for crystallization and therapeutics. *Protein Eng* **16**, 707-711 (2003). https://doi.org/10.1093/protein/gzg087

88 Yoshida, K. *et al.* The diabetogenic mouse MHC class II molecule I-Ag7 is endowed with a switch that modulates TCR affinity. *J Clin Invest* **120**, 1578-1590 (2010). https://doi.org/10.1172/JCI41502

89 Day, E. B. *et al.* Structural basis for enabling T-cell receptor diversity within biased virus-specific CD8+ T-cell responses. *Proc Natl Acad Sci U S A* **108**, 9536-9541 (2011). https://doi.org/10.1073/pnas.1106851108

90 Reeves, P. J., Callewaert, N., Contreras, R. & Khorana, H. G. Structure and function in rhodopsin: high-level expression of rhodopsin with restricted and homogeneous N-glycosylation by a tetracycline-inducible N-acetylglucosaminyltransferase I-negative HEK293S stable mammalian cell line. *Proc Natl Acad Sci U S A* **99**, 13419-13424 (2002). https://doi.org/10.1073/pnas.212519299

91 Moody, A. M., Xiong, Y., Chang, H. C. & Reinherz, E. L. The CD8alphabeta co-receptor on double-positive thymocytes binds with differing affinities to the products of distinct class I MHC loci. *Eur J Immunol* **31**, 2791-2799 (2001). https://doi.org/10.1002/1521-4141(200109)31:9<2791::aid-immu2791>3.0.co;2-x

92 Mallis, R. J. *et al.* Pre-TCR ligand binding impacts thymocyte development before alphabetaTCR expression. *Proc Natl Acad Sci U S A* **112**, 8373-8378 (2015). https://doi.org/10.1073/pnas.1504971112

93 Martin, M. Cutadapt removes adapter sequences from high-throughput sequencing reads. *2011* **17**, 3 (2011). https://doi.org/10.14806/ej.17.1.200

94 Langmead, B. & Salzberg, S. L. Fast gapped-read alignment with Bowtie 2. *Nat Methods* **9**, 357-359 (2012). https://doi.org/10.1038/nmeth.1923

95 Dobin, A. *et al.* STAR: ultrafast universal RNA-seq aligner. *Bioinformatics* **29**, 15-21 (2013). https://doi.org/10.1093/bioinformatics/bts635

96 Zhao, S., Ye, Z. & Stanton, R. Misuse of RPKM or TPM normalization when comparing across samples and sequencing protocols. *RNA* **26**, 903-909 (2020). https://doi.org/10.1261/rna.074922.120

97 Minor, W., Cymborowski, M., Otwinowski, Z. & Chruszcz, M. HKL-3000: the integration of data reduction and structure solution--from diffraction images to an initial model in minutes. *Acta Crystallogr D Biol Crystallogr* **62**, 859-866 (2006). https://doi.org/10.1107/S0907444906019949

98 Vagin, A. & Teplyakov, A. Molecular replacement with MOLREP. *Acta Crystallogr D Biol Crystallogr* **66**, 22-25 (2010). https://doi.org/10.1107/S0907444909042589

99 Emsley, P., Lohkamp, B., Scott, W. G. & Cowtan, K. Features and development of Coot. *Acta Crystallogr D Biol Crystallogr* **66**, 486-501 (2010). https://doi.org/10.1107/S0907444910007493

100 Afonine, P. V. *et al.* Towards automated crystallographic structure refinement with phenix.refine. *Acta Crystallogr D Biol Crystallogr* **68**, 352-367 (2012). https://doi.org/10.1107/S0907444912001308

101 Chen, V. B. *et al.* MolProbity: all-atom structure validation for macromolecular crystallography. *Acta Crystallogr D Biol Crystallogr* **66**, 12-21 (2010). https://doi.org/10.1107/S0907444909042073

102 Hwang, W. *et al.* CHARMM at 45: Enhancements in Accessibility, Functionality, and Speed. *J Phys Chem B* **128**, 9976-10042 (2024). https://doi.org/10.1021/acs.jpcb.4c04100

103 Eastman, P. *et al.* OpenMM 7: Rapid development of high performance algorithms for molecular dynamics. *PLoS Comput Biol* **13**, e1005659 (2017). https://doi.org/10.1371/journal.pcbi.1005659

Acknowledgments

We gratefully acknowledge Dr. Jia-huai Wang for carefully reviewing the manuscript. We thank Amelia Seabury for assistance with figure preparation. The use of SBC 19-ID at Argonne National Laboratory and the use of NYX 19-ID and FMX 17ID-2 at Brookhaven National Laboratory were supported by DOE contract no. DE-AC02-06CH11357 and DE-SC0012704, respectively. Monomers and tetramers listed in Supplementary Data 6 were obtained through the NIH Tetramer Core Facility. This work was supported by National Institutes of Health grant 1P01AI143565 (M.J.L, R.J.M, W.H, and E.L.R). Simulations were performed by using computers at the Texas A&M High Performance Research Computing facility.

Author contributions

A.A and K.T contributed to conceptualization, methodology, investigation, formal analysis, visualization, data curation, writing the original draft, and reviewing and editing the manuscript. R.J.M contributed to methodology, investigation, reviewing and editing the manuscript. M.A.B contributed to formal analysis, visualization, data curation, reviewing and editing the manuscript. J.S.D-C, contributed to methodology, investigation, formal analysis, visualization, data curation, reviewing and editing the manuscript. K.N.B contributed to methodology, investigation, formal analysis, visualization, reviewing and editing the manuscript. E.H.K contributed to methodology, investigation, formal analysis, and visualization. A.N.P contributed to methodology, formal analysis, visualization, reviewing and editing the manuscript. S.A contributed to investigation. V.C contributed to investigation and formal analysis. J.J.L, K.I.U, J.K.K, M.B, and C.M.M contributed to investigation. P.H.L contributed to data curation. M.Y.T contributed to data curation, supervision, reviewing and editing the manuscript. W.H contributed to formal analysis, Visualization, Funding acquisition, reviewing, and editing the manuscript. M.J.L contributed to conceptualization, visualization, funding acquisition, supervision, reviewing and editing the manuscript. E.L.R contributed to conceptualization, methodology, visualization, funding acquisition, supervision, writing the original draft, and reviewing and editing the manuscript.

Competing interests

Authors declare that they have no competing interests.

Materials & Correspondence

Supplementary Information is available for this paper. Correspondence and requests for materials should be addressed to: ellis_reinherz@dfci.harvard.edu, matt.lang@vanderbilt.edu.

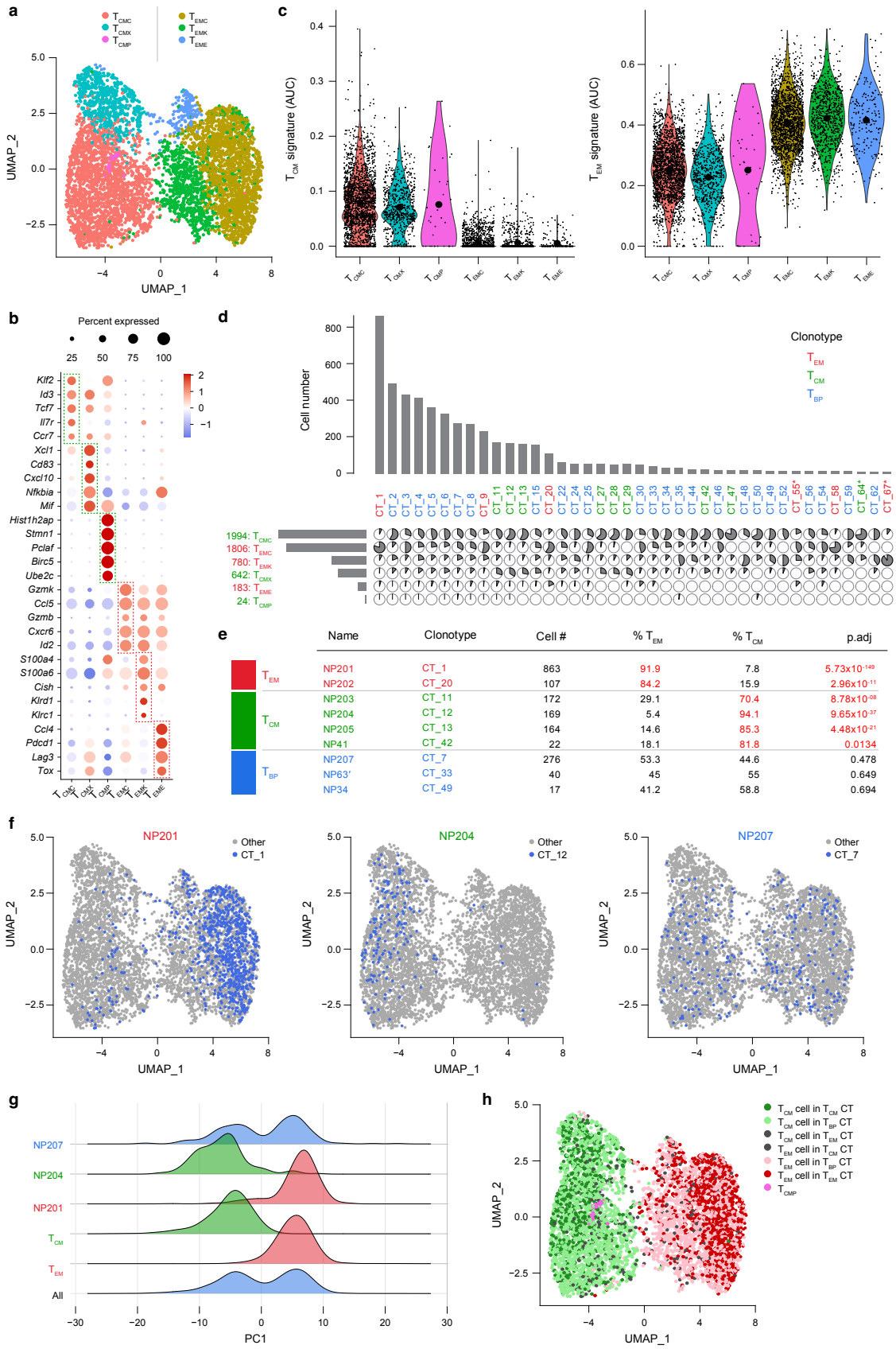
a
UMAP_2
UMAP_1
b
Percent expressed
25
50
75
100
Klf2
Id3
Tcf7
Il7r
Ccr7
Xcl1
Cd83
Cxcl10
Nfkbia
Mif
Hist1h2ap
Stmn1
Pclaf
Birc5
Ube2c
Gzmk
Ccl5
Gzmb
Cxcr6
Id2
S100a4
S100a6
Cish
Klrd1
Klrc1
Ccl4
Pdcd1
Lag3
Tox
c
T_CM signature (AUC)
T_EM signature (AUC)
d
Cell number
Clonotype
T_EM
T_CM
T_BP
1994: T_CMC
1806: T_EMC
780: T_EMK
642: T_CMX
183: T_EME
24: T_CMP
e
Name
Clonotype
Cell #
% T_EM
% T_CM
p.adj
NP201 CT_1 863 91.9 7.8 5.73x10^-149
NP202 CT_20 107 84.2 15.9 2.96x10^-11
NP203 CT_11 172 29.1 70.4 8.78x10^-08
NP204 CT_12 169 5.4 94.1 9.65x10^-37
NP205 CT_13 164 14.6 85.3 4.48x10^-21
NP41 CT_42 22 18.1 81.8 0.0134
NP207 CT_7 276 53.3 44.6 0.478
NP63' CT_33 40 45 55 0.649
NP34 CT_49 17 41.2 58.8 0.694
f
NP201
NP204
NP207
Other
CT_1
CT_12
CT_7
UMAP_2
UMAP_1
g
NP207
NP204
NP201
T_CM
T_EM
All
PC1
h
T_CM cell in T_CM CT
T_CM cell in T_BP CT
T_CM cell in T_EM CT
T_EM cell in T_CM CT
T_EM cell in T_BP CT
T_EM cell in T_EM CT
T_CMP
UMAP_2
UMAP_1

Fig. 1. TCRαβ clonotypes intrinsically influence memory CD8$^+$ T cell fate. a, UMAP clustering of $NP_{366-374}$-specific memory CD8$^+$ T cells. **b,** Dotplot of select immune-related genes. Circles are proportional to the fraction of cells with expression of the indicated gene. Red indicates high expression relative to other clusters while blue indicates low expression. **c,** Violin plots of T_{CM} and T_{EM} gene signatures generated from an independent experiment and applied to the six clusters. The black dots show the medians. **d,** Correlation matrix of the 40 most abundant clonotypes. Pie slice sizes are proportional to the fraction of the clonotype in each cluster. The barplot above the matrix indicates the number of cells with the given clonotype while the barplot to the left indicates the number of cells in each cluster. **e,** Table of select clonotypes and their distribution across T_{CM} and T_{EM} clusters. T_{CM} and T_{EM} clonotypes are those for which more than 70% of cells are in T_{CM} or T_{EM} cluster, respectively. T_{BP} clonotypes are those for which fewer than 70% of cells are in a T_{CM} or T_{EM} cluster. P-values were generated using a binomial test (with adjustment by the Benjamini-Hochberg procedure) relative to the overall distribution T_{CM} or T_{EM} cells. The prime (‘) dictates the usage of TRAV16 for CT_33, which differs at two residues from TRAV16N used by NP63 (V→ M and V→ E) at sites distal to the pMHC interface. **f,** Blue dots on UMAPs showing which cells bear the indicated clonotypes. **g,** Ridge plot indicating the position of cells across the first principal component. Sets of cells include all cells, cells from T_{CM} clusters, T_{EM} clusters, and select clonotypes. **h,** UMAP with cells colored by the indicated CT category and memory cell types comprising each. T_{CM} and T_{EM} cells are cells in a T_{CM} or T_{EM} cluster, respectively.

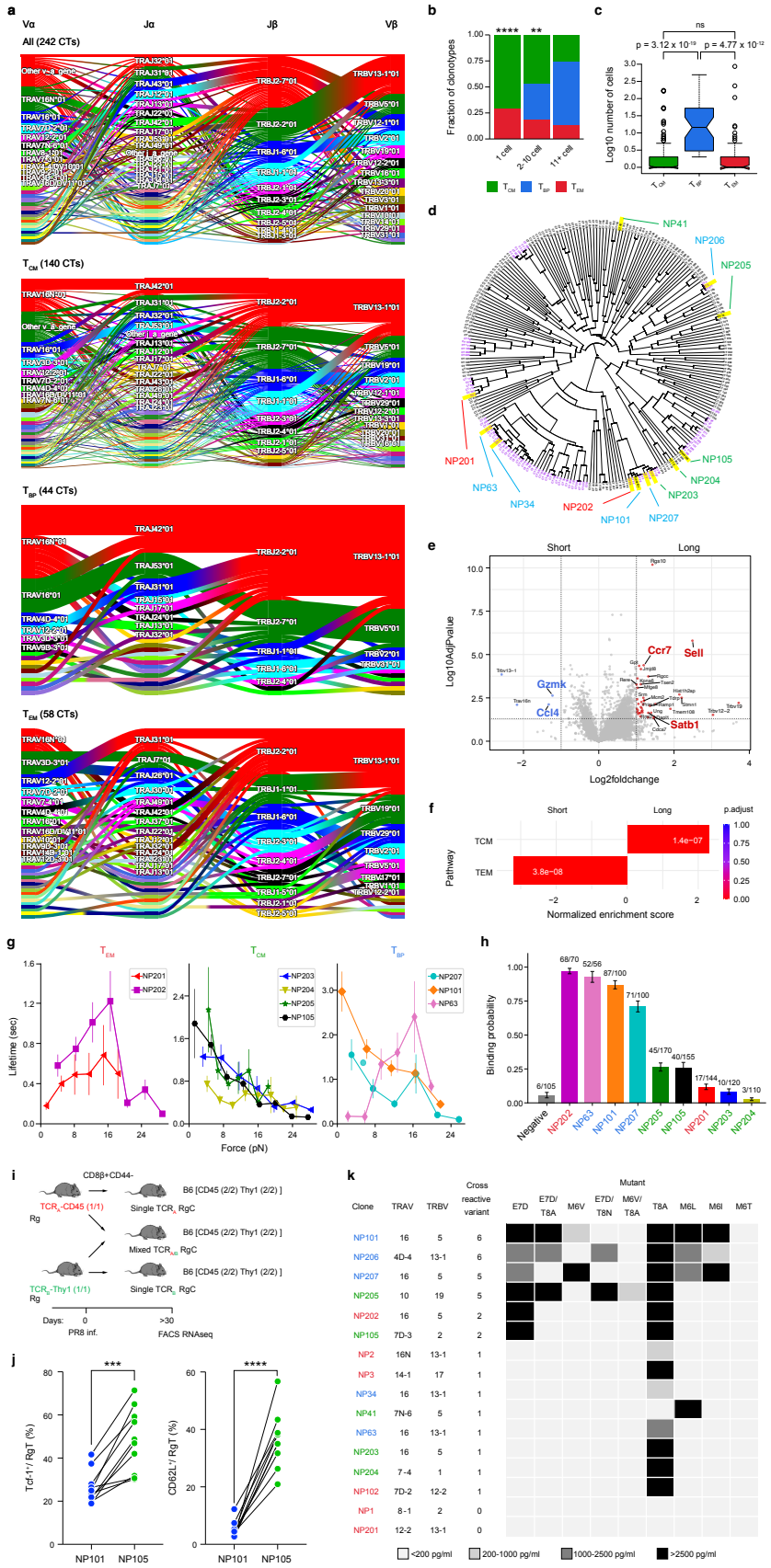
a
Vα
Jα
Jβ
Vβ
All (242 CTs)
T_CM (140 CTs)
T_BP (44 CTs)
T_EM (58 CTs)
b
Fraction of clonotypes
1 cell
2-10 cell
11+ cell
c
Log10 number of cells
ns
p = 3.12 x 10^-19
p = 4.77 x 10^-12
d
NP41
NP206
NP205
NP201
NP63
NP34
NP202
NP101
NP207
NP105
NP204
NP203
e
Short
Long
Log10AdjPvalue
Log2foldchange
Ccr7
Sell
Gzmk
Ccl4
Satb1
f
Short
Long
p.adjust
Pathway
TCM
TEM
1.4e−07
3.8e−08
Normalized enrichment score
g
T_EM
T_CM
T_BP
Lifetime (sec)
Force (pN)
NP201
NP202
NP203
NP204
NP105
NP207
NP101
NP63
h
Binding probability
6/105
68/70
52/56
87/100
71/100
45/170
40/155
17/144
10/120
3/110
Negative
NP202
NP63
NP101
NP207
NP205
NP105
NP201
NP203
NP204
i
CD8β+CD44-
TCRα-CD45 (1/1)
Rg
Single TCRα RgC
B6 [CD45 (2/2) Thy1 (2/2)]
Mixed TCRαβ RgC
TCRβ-Thy1 (1/1)
Days:
0
>30
PR8 inf.
FACS RNAseq
j
Tcf-1+/ RgT (%)
CD62L+/ RgT (%)
NP101
NP105
k
Clone
TRAV
TRBV
Cross reactive variant
E7D
E7D/ T8A
M6V
E7D/ T8N
M6V/ T8A
T8A
M6L
M6I
M6T
Mutant
NP101 16 5 6
NP206 4D-4 13-1 6
NP207 16 5 5
NP205 10 19 5
NP202 16 5 2
NP105 7D-3 2 2
NP2 16N 13-1 1
NP3 14-1 17 1
NP34 16 13-1 1
NP41 7N-6 5 1
NP63 16 13-1 1
NP203 16 5 1
NP204 7-4 1 1
NP102 7D-2 12-2 1
NP1 8-1 2 0
NP201 12-2 13-1 0
<200 pg/ml
200-1000 pg/ml
1000-2500 pg/ml
>2500 pg/ml

Fig. 2. Distinct features of memory T cells according to their polarities. a, Sankey plot of V and J-gene usage by clonotype category. **b,** Stacked barplot of clonotype type distribution binned by cell number. The p-values by chi-squared test for comparison between T_{CM} and T_{EM} are: 1 cell vs overall distribution of cells: ****; $p = 7.58 \times 10^{-7}$, 2-10 cells: **; p = 0.0093, and 11+ cells: p = 0.29. **c,** Boxplot of cell number by clonotype type. P-values for comparisons were calculated by Mann-Whitney-U test. **d,** Phylogram of clonotypes generated by hierarchical clustering of TCR distances with complete linkage. Clonotypes that are sequence similar to multiple other clonotypes ("short branch") are shaded in purple while the remaining clonotypes ("long branch") are in black. Representative T_{EM} clonotypes are highlighted in red, T_{CM} in green, and T_{BP} in blue. **e,** Volcano plot of differential expression of clonotypes in the long branch category versus short branch category. **f,** Gene Set Enrichment Analysis of the differential expression in E using the T_{CM} and T_{EM} gene signatures. **g,** Force vs. lifetime plot for T_{EM} clones NP201 (red curve, N=56), NP202 (magenta curve, N=136); T_{CM} clones NP203 (blue curve, N=58), NP204 (yellow curve, N=110), NP205 (green curve, N=79), NP105 (black curve, N=101); and T_{BP} clones NP101 (orange curve, N=103), NP207 (cyan curve, N=100) And NP63 (pink curve, N=40) with its cognate ligand NP366-374/Db. Error bars indicate SEM. **h,** Tether forming probability for the SM optical tweezers assay under identical conditions of tethers per bead and surface ligand density. Error bars indicate SEM. **i,** Experimental scheme for generating single and mixed retrogenic (RgC) mice using congenic markers (i.e., CD45.1/1, CD45.1/2 or Thy1.1) is detailed in Methods. **j,** Tcf-1 and CD62L expression on Rg T cells in mLN of mixed NP101/105 RgC mice that were recipients of 5,000 Rg T cells bearing each clonotype (i.e. 10,000 cells total). **k,** Crossreactivity profiles of 16 NP-specific TCRs against a panel of naturally occurring IAV variants carrying mutated NP peptides. Reactivity was assessed by measuring IL-2 production from TCR-transduced BW cell lines following stimulation with peptide-loaded APC. Memory category color coding matches that in **d**. Data is the representative of two or three independent experiments.

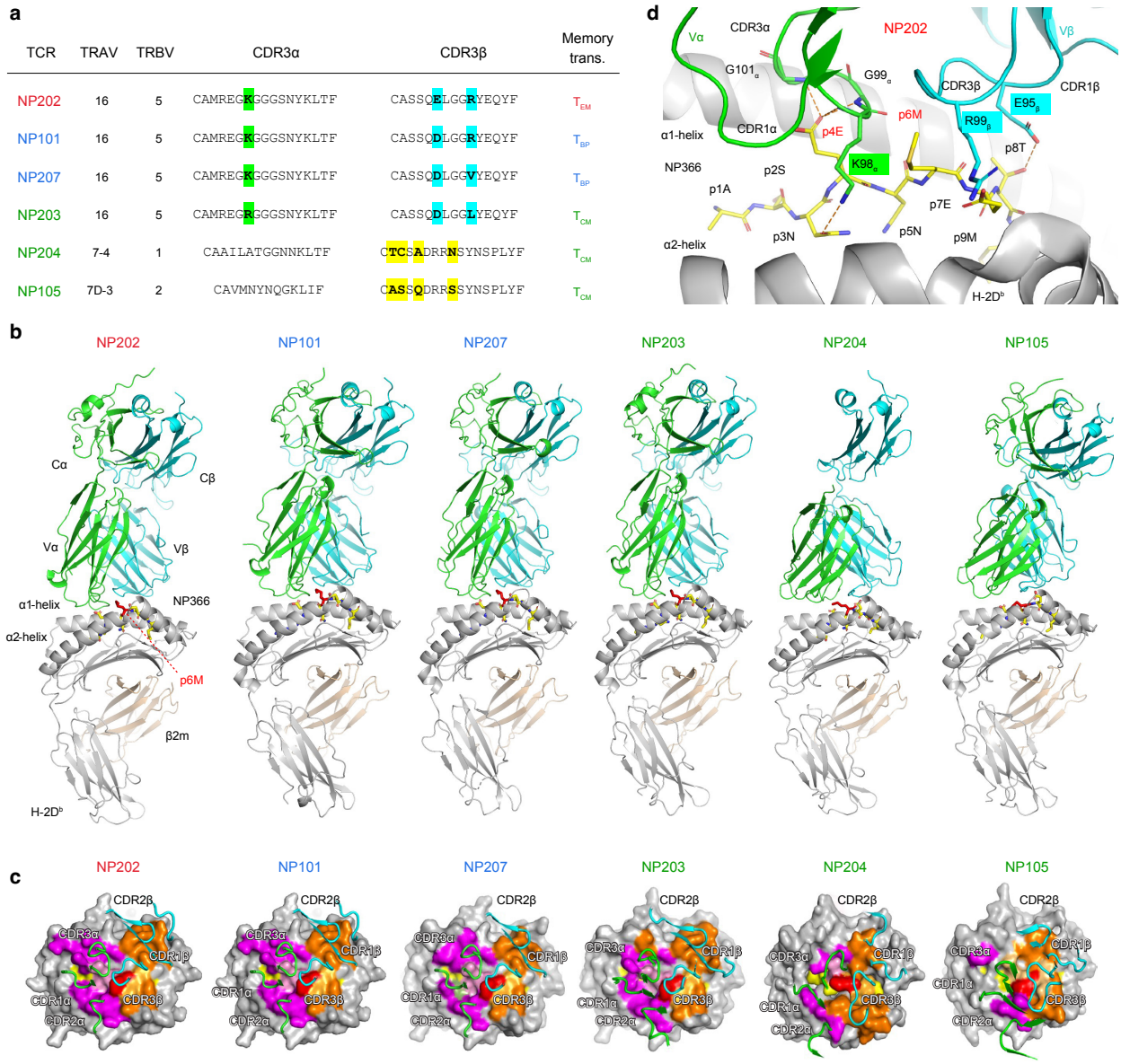

Fig. 3. TCR sequences and structures of six NP TCR-NP$_{366-374}$/D^b complexes derived from T$_{EM}$, T$_{CM}$ and T$_{BP}$ memory CD8 T cells. a, The genes and CDR3 sequences of six NP TCRs. In the first four NP TCRs, the three residues that vary among their CDR3s are highlighted in green or cyan. Between NP105 and NP204 key CDR3β residues are in common as a result of a shared TRBJ1-6. Only varied residues between two CDR3β are highlighted in yellow. **b,** Ribbon diagrams of six NP TCR-NP$_{366-374}$ /D^b complexes arranged in the order from T$_{EM}$ (α-dominant) to T$_{CM}$ (β-dominant) from left to right. Their α1α2 domains of MHC are positioned in the same orientation. The NP$_{366-374}$ peptide is displayed in sticks with the central residue p6M highlighted in red. TCR Vα, TCR Vβ, NP$_{366-374}$ peptide, MHC α chain and MHC β$_{2m}$ are colored in green, blue, yellow, grey and light orange, respectively. The Cα domain of NP 204 TCR is absent due to structural disorder. **c,** TCR CDR loops and their footprints on pMHC. Magenta and pink surface areas

represent the MHC and peptide residues that interact with TCR Vα, respectively. Orange and bright orange surface represent the MHC and peptide residues that interact with TCR Vβ, respectively. **d,** A zoomed-in view of the interaction between TCR and peptide in the NP202-$NP_{366-374}$ complex. The three varied CDR3 residues noted in **a** are highlighted in the same color schemes to show their positions and roles. All peptide residues are labeled, with p4E and p6M highlighted in red for their prominent roles in TCR's recognition.

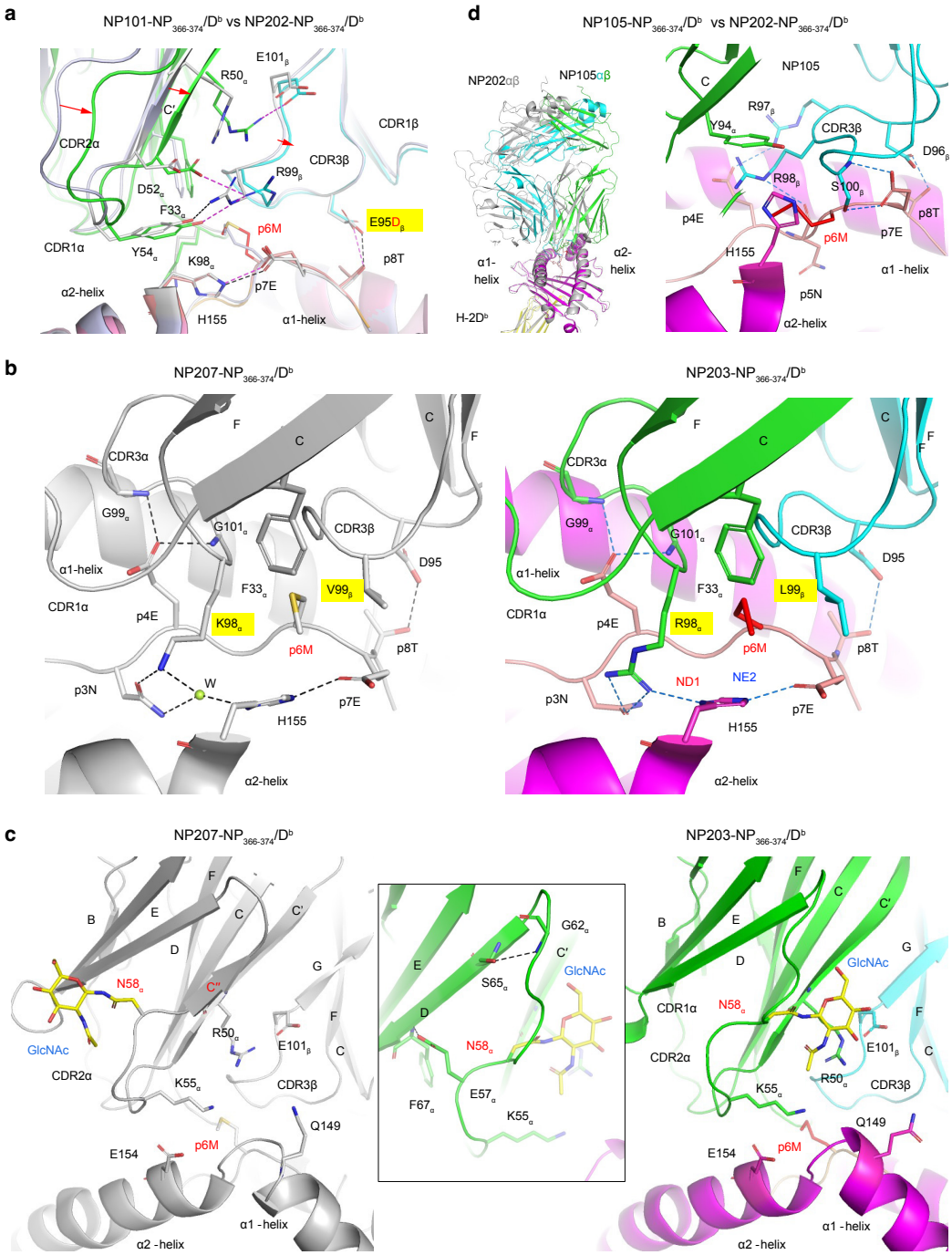

Fig. 4. Fine structure details of TCR-ligand interactions in a single CD8 T cell repertoire linked to memory differentiation. **a,** TCR-pMHC interface area of NP101 and NP202 complexes superimposed based on their D^b α1α2 MHC domains. The NP202 complex is colored in grey as a reference. The TCR α-chain, TCR β-chain, peptide and MHC of NP101 complex are colored in green, cyan, orange and pink, respectively. A few relevant residues are displayed in sticks for comparison. **b,** Side-by-side comparison between NP207 and NP203 complexes. NP207 complex

is colored in grey on the left. The TCR α-chain, TCR β-chain, peptide and MHC of NP203 complex are colored in green, cyan, pink and magenta, respectively. Some key residues described in text are shown in sticks to display hydrogen bonds and salt bridges. The ND1 and NE2 atoms of H2-D^b H155 are labeled to show their potential pronation/deprotonation status. **c,** Side-by-side comparison between NP207 and NP203 complexes in a view focusing on the C'(C")-D edge of Vα domain. The NAG moiety attached to N58α is shown in sticks. In NP203 complex, the extended loop between C' strand and D strand is stabilized by two hydrogen bonds between sidechain and mainchain as shown in the insert. **d,** A docking comparison of β-dominated NP105 (in grey) with α-dominated NP202 (colored) on the left and a zoomed-in display of NP105 interaction with $NP_{366-374}$ /D^b on the right, in which a part of α2-helix in front of peptide is omitted for clarity.

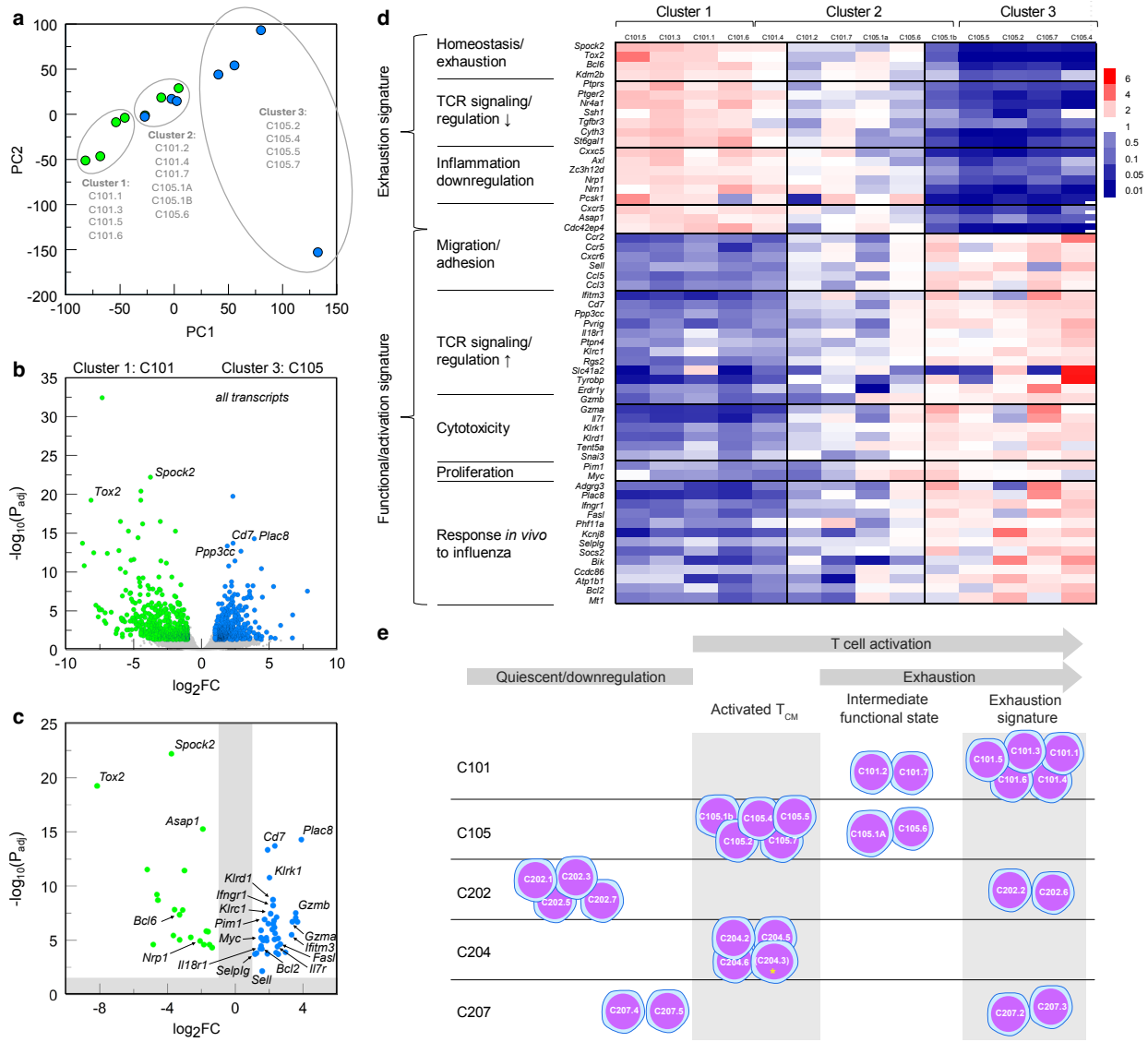

Fig. 5. Functional characterization by transcriptome of Rg T cells isolated from mediastinal lymph nodes of IAV-infected host animals. a, PCA for gene expression of Rg mLN-derived T cells from B6 mice adoptively transferred with either 10^5 C101 (green) or C105 (blue) retrogenic $CD8^+$ T cells expressing NP101 or NP105 TCRs, respectively, 30 d after IAV infection. Each data point represents results from an individual mouse (n = 14 mice). **b,** Volcano plot of significant differential gene expression (962 genes) between Cluster 1 Rg cells (all C101, green) and Cluster 3 (all C105, blue). **c,** Volcano plot of a 59 differentially expressed gene subset flagged for known T cell functionality (T cell panel) where Cluster 1 (C101.n) exhibits an "exhausted" signature and Cluster 3 (C105.n) exhibits a functionally activated T_{CM} transitioning to T_{EM} signature. **d,** Hierarchical clustering/heat map of 59 gene T cell panel reclusters samples to 5 exhibiting an "exhausted" signature (all C101), 5 with activated T_{CM} signature (all C105), and a mixed C101/C105 cluster of 4 with an intermediate signature. Each row scaled where 1 (white) = base gene mean, red = fold-change above, and blue = fold-change below, the base mean. **e,** Schematic of merged C100.n [expressing NP101 and NP105 TCRs] and C200.n [expressing NP202, NP204,

1579 and NP207 TCRs] samples (see Extended Data Fig. 10), shows skewed distribution of clonotypic
1580 Rg T cells by exhaustion signature, activated T_{CM} functionality, and activation state (n = 28 RNA-
1581 seq analyses). The asterisk for C204.3 indicates quiescent signature by activation state (Extended
1582 Data Fig. 10c) but T_{CM} signature by differential T cell panel (Extended Data Fig. 10d).
1583

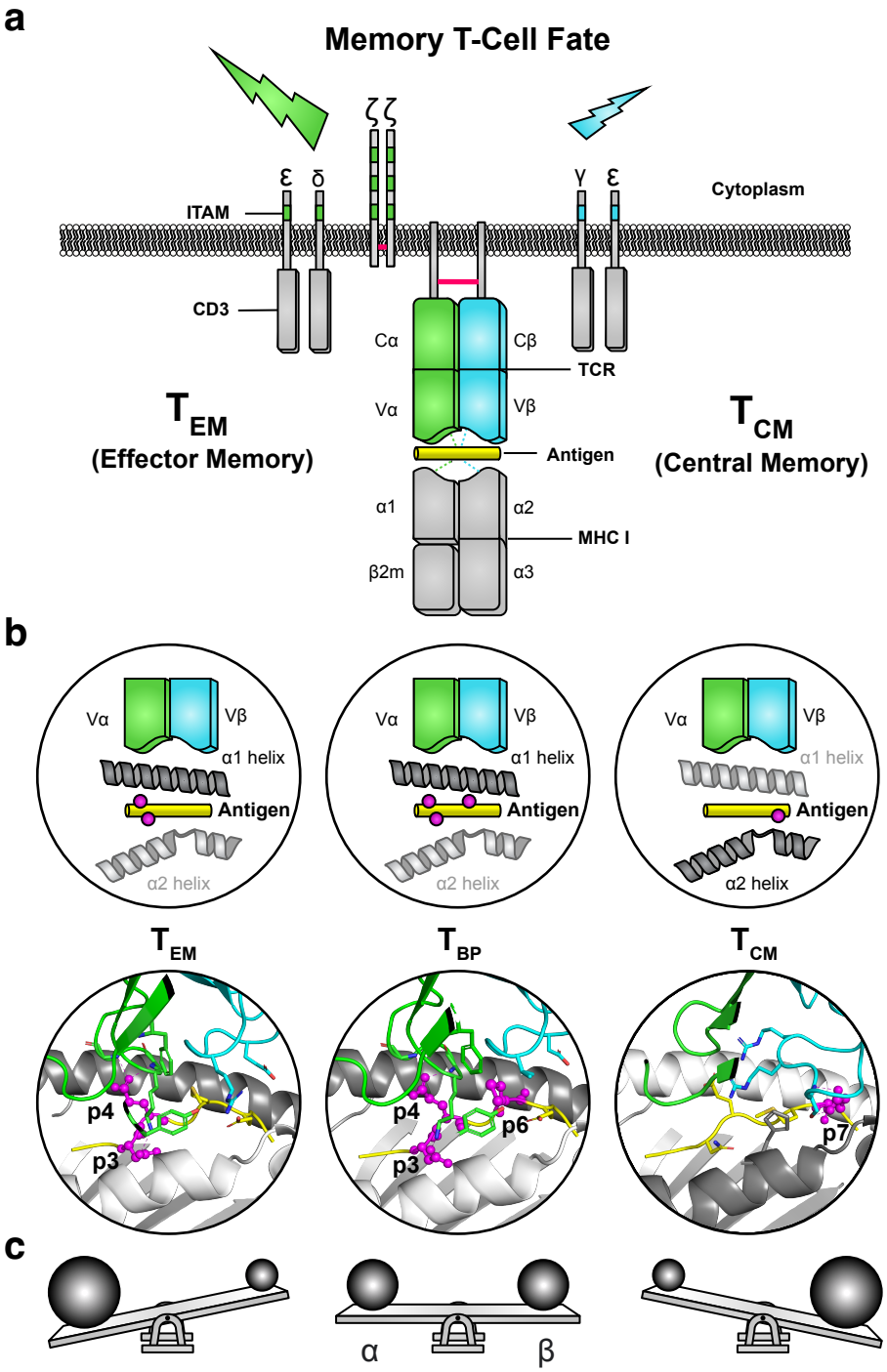

Fig. 6. Schematic representation of memory T-cell fate and relationships to signaling balance or asymmetry. a, Differential signaling related to TCR sidedness as a cartoon representation with CD3 elements and their ITAMs exposed to yield activation as shown. **b,** Graphic depicting key peptide residues involved in TCR interaction illustrated as magenta balls on the peptide backbone (simple cylinder) that sits in the antigen presenting platform between the labeled MHC helices in the top row. The bottom row shows graphics based upon X-ray crystallographic structures of those residues in magenta ball and stick display with CDR3α and CDR3β (green and cyan) at the top.

1593 Both rows are based on the TCRs NP202, NP207, and NP105 from left to right. Other neighboring
1594 residues are not labeled for clarity. In both rows, the MHC helix closest to the mass center of the
1595 TCR is indicated by the dark color in each complex. **c,** Force on the TCRα and TCRβ subunits are
1596 balanced for T_{BP}, in contrast to the indicated imbalances associated with T_{EM} and T_{CM} represented
1597 as balls of equivalent or differing sizes on a seesaw in gravitation pull to the ground. With respect
1598 to TCR mechanobiology, however, the seesaws would be flipped as the balls represent sizes of
1599 pMHC-related forces impacting the indicated TCR subunits.
1600